New Journal of Physics
The open-access journal for physics

Modified spin-wave theory with ordering vector optimization: spatially anisotropic triangular lattice and $J_1 J_2 J_3$ model with Heisenberg interactions

Philipp Hauke[1,6], Tommaso Roscilde[2], Valentin Murg[3], J Ignacio Cirac[4] and Roman Schmied[5]

[1] ICFO—Institut de Ciències Fotòniques, Av. Canal Olímpic s/n, E-08860 Castelldefels (Barcelona), Spain
[2] Laboratoire de Physique, Ecole Normale Supérieure de Lyon, 46 Allée d'Italie, F-69007 Lyon, France
[3] Fakultät für Physik, Universität Wien, Boltzmanngasse 3, A-1090 Vienna, Austria
[4] Max-Planck-Institut für Quantenoptik, Hans-Kopfermann-Strasse 1, D-85748 Garching, Germany
[5] Departement Physik, Universität Basel, Klingelbergstrasse 82, CH-4056 Basel, Switzerland
E-mail: Philipp.Hauke@icfo.es

New Journal of Physics **13** (2011) 075017 (29pp)
Received 20 December 2010
Published 29 July 2011
Online at http://www.njp.org/
doi:10.1088/1367-2630/13/7/075017

Abstract. We study the ground-state phases of the $S = 1/2$ Heisenberg quantum antiferromagnet on the spatially anisotropic triangular lattice (SATL) and on the square lattice with up to next-next-nearest-neighbor coupling (the $J_1 J_2 J_3$ model), making use of Takahashi's modified spin-wave (MSW) theory supplemented by ordering vector optimization. We compare the MSW results with exact diagonalization and projected-entangled-pair-states calculations, demonstrating their qualitative and quantitative reliability. We find that the MSW theory correctly accounts for strong quantum effects on the ordering vector of the magnetic phases of the models under investigation: in particular, collinear magnetic order is promoted at the expense of non-collinear (spiral) order, and several spiral states that are stable at the classical level disappear from the quantum phase diagram. Moreover, collinear states and non-collinear ones are never connected continuously, but they are separated by parameter regions in

[6] Author to whom any correspondence should be addressed.

which the MSW theory breaks down, signaling the possible appearance of a non-magnetic ground state. In the case of the SATL, a large breakdown region appears also for weak couplings between the chains composing the lattice, suggesting the possible occurrence of a large non-magnetic region continuously connected with the spin-liquid state of the uncoupled chains. This shows that the MSW theory is—despite its apparent simplicity—a versatile tool for finding candidate regions in the case of spin-liquid phases, which are among prime targets for *relevant* quantum simulations.

Contents

1. Introduction

Low-dimensional frustrated quantum spin systems can display an intriguing interplay between order and disorder: classical order has been shown to be quite resilient in two or three dimensions [1–4]; frustration, however, can lead to the melting of magnetic long-range order (LRO) and the emergence of quantum-disordered states like valence-bond solids or resonating valence-bond states [5, 6]. Understanding such magnetically disordered quantum phases is important for the search for fractionalized excitations in two dimensions [5], as well as for the understanding of the behavior of layered magnetic insulators/metals in which magnetism is disrupted by charge doping, leading to dramatic phenomena such as superconductivity at high critical temperature [7–9]. It is hoped that quantum simulators, i.e. well-controlled quantum devices specifically constructed to behave as a given model system, can help to further our understanding of magnetic quantum phases.

A large variety of magnetic materials can be described by the Heisenberg Hamiltonian

$$H_{\mathrm{S}} = \sum_{i,j} J_{ij}\, \boldsymbol{S}_i \cdot \boldsymbol{S}_j, \tag{1}$$

where $\boldsymbol{S}_i$ is a quantum spin-S operator at site i. In this paper, we will focus on the antiferromagnetic case for $S = 1/2$, and on two-dimensional (2D) frustrated lattices.

Quasi-2D frustrated antiferromagnetism is relevant to a variety of $S = 1/2$ compounds, realizing the spatially anisotropic triangular lattice (e.g. in Cs_2CuCl_4 [10] and κ-(BEDT-TTF)$_2$Cu$_2$(CN)$_3$ [11, 12], etc), or the frustrated ($J_1 J_2$) square lattice (e.g. in $Li_2VOSi(Ge)O_4$, $VOMoO_4$ [13], $BaCdVO(PO_4)_2$ [14], etc). For both lattice geometries, the Heisenberg model is expected to display spin-liquid phases for particular values of the frustrated couplings, although the extent and nature of these spin-liquid phases is still under theoretical debate, both for the spatially anisotropic triangular lattice (SATL) [15–21] and for the frustrated square lattice [22–28].

In this work, we investigate the $S = 1/2$ Heisenberg antiferromagnetic Hamiltonian on 2D frustrated lattices making use of Takahashi's modified spin-wave (MSW) theory [29], supplemented with the optimization of the ordering vector [30]. In a previous paper [31], we have shown that (for the SATL with XY interactions) this approach provides a significant improvement over conventional spin-wave theory (as well as over the conventional MSW theory), as it allows one to correctly account for the dramatic quantum effects occurring to the form of order that appears in frustrated quantum antiferromagnets, and for the quantum corrections to the stiffness of the ordered phase. In particular, a very low stiffness, or the complete breakdown of the theory, provide strong signals that the true ground state might be quantum disordered; hence, this method serves as a viable approach to finding candidate models potentially displaying spin-liquid behavior. For a more detailed description of the formalism, we refer the reader to [31].

Here, we apply this MSW theory with ordering vector optimization to the Heisenberg SATL, as well as to the square lattice with nearest, next-to-nearest (NNN) and next-to-next-to-nearest-neighbor (NNNN) couplings (the $J_1 J_2 J_3$ model [27], [32–34]). Both models feature a very complex $T = 0$ phase diagram, with spirally and collinearly ordered regions, whose ordering vector is subject to strong quantum corrections with respect to the classical ($S \to \infty$) limit. They also feature extended breakdown regions for the MSW theory, pointing at the possible spin-liquid nature of the true ground state of the system. Comparison with numerical results coming from exact diagonalization (ED) and projected-entangled-pair-state (PEPS) calculations show that the MSW theory correctly accounts for some of the most salient features of the quantum phase diagram of these systems, and that it hence represents a very versatile tool to probe the robustness (or the breakdown) of a semi-classical description of the ground state of frustrated quantum magnets. As such, it requires a relatively low effort to find parameter regions that might harbor exotic quantum phases, and that are therefore good candidates for useful application of a quantum simulator.

The remainder of this paper is organized as follows: section 2 presents the ground-state phase diagram of the SATL with nearest-neighbor Heisenberg interactions; in section 3, we calculate the ground-state phase diagram of the $J_1 J_2 J_3$ model; finally, in section 4 we present our conclusions. The technical aspects of the MSW theory applied to Heisenberg antiferromagnets are presented in the appendix.

2. Modified spin-wave theory on the spatially anisotropic triangular lattice with nearest-neighbor Heisenberg bonds

The triangular lattice with Heisenberg interactions has been considered as one of the first candidate systems for quantum-disordered behavior in the ground state [5]. Recently, the phase diagram of the SATL up to values of $\alpha \equiv J'/J = 1$ (where J is associated with bonds along the e_x coordinate vector, and J' with bonds along the $1/2e_x \pm \sqrt{3}/2e_y$ vectors; see figure 1(a))

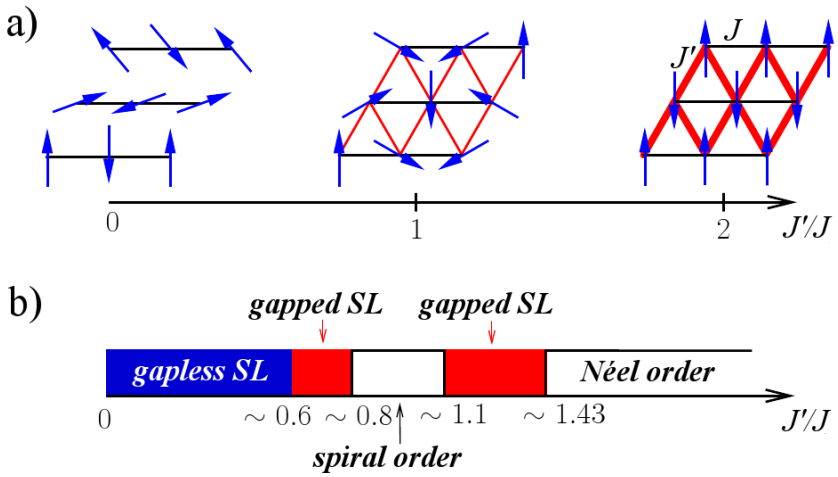

Figure 1. (a) Classical ground-state phase diagram of the SATL with a sketch of the 1D state at $\alpha \equiv J'/J = 0$, the spiral state at $\alpha = 1$ and the 2D-Néel state for $\alpha \geqslant 2$. (The horizontal black bonds have strength J, and the diagonal red bonds have strength J'.) (b) The quantum mechanical phase diagram changes considerably due to order-by-disorder effects and the appearance of spin liquids [15, 16].

has been studied by Yunoki and Sorella using variational quantum Monte Carlo (VMC) methods [16]. They find that the gapless spin-liquid phase of the isolated chains ($J' = 0$) persists also at finite coupling up to a critical value $\alpha \approx 0.65$, followed by a gapped spin liquid; for $\alpha \approx 0.8$ the gap closes and the system undergoes an ordering transition to spiral order, continuously connected with the three-sublattice order of the isotropic Heisenberg antiferromagnet ($\alpha = 1$). This scenario is still controversial, however: studies based on low-energy effective field theory for the description of the coupled chains in the case $\alpha < 1$ indicate that the system might still exhibit long-range antiferromagnetic order even for very weak coupling among the chains. This form of order results from high-order perturbation theory in the inter-chain coupling, and it is necessarily very weak, given that numerical methods cannot detect it. Its observation is clearly beyond the capabilities of our MSW approach. Coming from the large-α limit, series expansions by Weihong *et al* indicate that 2D-Néel order—appearing on the square lattice defined by the dominant J'-couplings—persists down to $\alpha \simeq 1.43$, followed by a phase without magnetic order in the interval $1.1 \lesssim \alpha \lesssim 1.43$ [15]. Below this region the authors find incommensurate spiral order connecting continuously to the isotropic point $\alpha = 1$. In [35], qualitative similar results have been obtained using the Schwinger-boson approach. The resulting phase diagram differs strongly from the classical one, which is characterized by spiral order for $0 < \alpha < 2$, and by Néel order for $\alpha \geqslant 2$. The classical phase diagram is contrasted with the quantum mechanical one (composed from [15] and [16]) in figure 1. It is interesting to notice that a qualitatively similar phase diagram has been obtained recently by some of us for the XY model on the SATL [31, 36].

A variety of experiments have been performed on magnetic compounds described by the Heisenberg model on the SATL, with results that are still controversial. For instance, neutron scattering experiments of Coldea *et al* [10] on Cs_2CuCl_4, where $\alpha \approx 1/3$, claimed evidence that the low-energy physics is governed by spinons, fractionalized excitations with $S = 1/2$, which

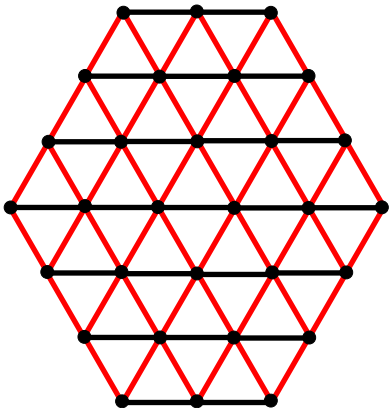

Figure 2. Cluster of 30 spins for which we carried out ED. The 24-spin system is equivalent, only with the top and bottom rows removed. Black dots denote sites, the horizontal black bonds have strength J, and the diagonal red bonds have strength J'.

represent the elementary excitations in the case of uncoupled chains. Yet, Kohno *et al* [19] showed that, for finite inter-chain coupling, spinons tunnel between chains in bound pairs with $S = 1$ (the so-called triplons), so that the fractionalization in two dimensions is, strictly speaking, not present. Kohno *et al* [19] argue that the spinons in Cs_2CuCl_4 are descendants of the excitations of the individual 1D chains and not characteristic of any exotic 2D state. This further reinforces the idea of quasi-1D behavior up to relatively high inter-chain interactions mentioned in the previous paragraph.

2.1. MSW predictions for the ground-state phase diagram

In this section, we discuss the ground-state phase diagram resulting from the predictions of MSW theory for the $S = 1/2$ SATL with nearest-neighbor (NN) Heisenberg interactions (see the appendix for technical details).

In order to assess the validity of MSW results, we compare them with EDs. Using the Lanczos method, we compute the ground state of small clusters of 14, 24 and 30 spins. The considered geometry for the 30-spin system can be found in figure 2. The 24-spin system can be obtained from it by removing the top and bottom rows. The 14-spin cluster is an equivalent system with rows of 2, 3, 4, 3 and 2 spins. The clusters are chosen for their symmetry with respect to reflection along the coordinate axis, and for their ratio of the number of J'-bonds (red) to the number of J-bonds (black), which lies close to the bulk value of 2. We use open boundary conditions to allow for the accommodation of spiral order with arbitrary wave vector.

We find that, due to the peculiar geometries chosen, there exist parameter ranges where the ground state falls into the threefold degenerate triplet with total spin equal to unity. Nonetheless, we restrict our calculations to the $M_z^{\text{total}} = 0$ subspace (with M_z^{total} being the z-component of the total spin), and the $M_z^{\text{total}} = \pm 1$ states are excluded. This results in an apparent breaking of the x–z symmetry (the x–y symmetry is preserved). This symmetry would be recovered by averaging over the whole triplet subspace. The reason for such an apparent symmetry breaking resides in the particular geometry of the cluster considered, which complicates the comparison between different system sizes. This triplet physics might play an important role in the case of

bigger systems, although one cannot draw conclusions about the thermodynamic limit from the small clusters considered. A non-trivial triplet physics could especially be an issue for variational methods restricting their focus to the singlet subspace.

The MSW results are computed in the infinite lattice limit, which is achieved by transforming in equations (A.6) and (A.7) the sums over the first Brillouin zone into integrals.

2.1.1. Parameter regions where MSW theory fails to converge. Convergence in the self-consistent equations of MSW theory with ordering vector optimization, equations (A.3)–(A.7), (A.9), cannot be achieved in selected regions of the ground-state phase diagram, namely for $\alpha \lesssim 0.65$ and for $1.14 \lesssim \alpha \lesssim 1.3$. (Interestingly, convergence is restored in the pure 1D limit, $\alpha = 0$, for which the theory formulates surprisingly good predictions.) This breakdown of convergence corresponds to the appearance of an imaginary part in the spin-wave frequencies, equation (A.5), signaling an instability of the ordered ground state. The breakdown of a self-consistent description of the system in terms of an ordered ground state is strongly suggestive of the presence of a quantum-disordered ground state in the exact behavior of the system. Hence, one can interpret these parameter regions as candidates for the spin liquids predicted from [15, 16] (compare figure 1(b)). Both for $\alpha < 1$ and $\alpha > 1$, we find that the breakdown region of MSW appears to be fully contained within the region of SL behavior (either gapped or gapless) estimated in [15, 16]. Hence MSW theory is seen to possibly underestimate the width of the quantum-disordered regions in the phase diagram, which is to be expected due to the partial account of quantum fluctuations given by the MSW theory.

2.1.2. MSW ground-state energy in comparison with previous results. Table 1 demonstrates that the energy from the MSW theory compares very well with results that were obtained recently by Yunoki and Sorella by VMC methods [16], also plotted in figure 3. For comparison, we also show the curve that they obtain with a projected-BCS (p-BCS) wave function.

In the isotropic triangular lattice, the MSW energy compares also favorably to the data from the Green's function Monte Carlo method with stochastic reconfiguration (GFMCSR) from [40], but both energy and order parameter (see section 2.1.3) lie closest to the VMC calculation from Weber *et al* [38], who used a mixture of a BCS wave function and a wave function with spiral order as their starting point (BCS+spiral). The MSW theory predicts a smaller energy than the LSW theory as well as 1/S expansion [44, 45], but since neither of these methods is variational this does not rigorously mean that the MSW ground state is better.

At $\alpha = 0$, the MSW value $E_0(\alpha = 0) = -0.4647$ is relatively close to the exact result of the 1D case, $-(\ln 2 - 1/4) = -0.443\,15$. However, it is located *below* the exact value. Again, this apparent puzzle is resolved by noting that the MSW method is not variational due to the incomplete inclusion of the kinematic constraint (see the appendix). We also note that the ground-state energies derived from ED of the 30-site system lie very close to the values from the other methods except in the 1D phase. This could be attributed to the small system size: if the interpretation is correct that for small α the Heisenberg SATL is in a 1D-like phase with algebraic correlations, it is natural that finite-size effects play a very important role in the critical 1D phase. This would explain the strong deviation of the ED energy in that parameter region.

On the square lattice ($\alpha \to \infty$), Takahashi showed already 20 years ago the extremely good performance of the MSW theory [29]: its ground-state energy per spin is -0.6699, which is in excellent agreement with the QMC result $-0.669\,437(5)$ [42].

New Journal of Physics **13** (2011) 075017 (http://www.njp.org/)

IOP Institute of Physics DEUTSCHE PHYSIKALISCHE GESELLSCHAFT

Table 1. Comparison of the ground-state energy per spin derived by various methods, for some values of α. VMC stands for 'variational quantum Monte Carlo' where the wave function used is given in brackets. FN is short for lattice fixed node and FNE for the improved FN effective Hamiltonian method. SBMFT is short for Schwinger-boson mean-field theory, and GFMCSR stands for Green's function Monte Carlo method with stochastic reconfiguration. Also included are the exact result of the Heisenberg chain ($\alpha = 0$) in the thermodynamic limit, which can be computed using a Jordan–Wigner transform, the ED results for the 30-spin cluster and the ED results from finite-size extrapolations of calculations on clusters of up to 40 spins. The last column shows the staggered magnetization or, in the case of MSW theory, the population of the zero mode M_0.

Method	$\alpha = 0$	$\alpha = 0.7$	$\alpha = 0.8$	$\alpha = 1$	$\alpha = \infty$	M at $\alpha = 1$
exact, thermodynamic limit	−0.443 147					
exact, $N = 30$ (present study)	−0.412 7			−0.547 1		0.131 4
exact, $N = 40$, extrapolated [37]					−0.670 1	
VMC (RVB) [16]				−0.512 3(1)		0.0
VMC (RVB with $\mu = 0$) [16]				−0.529 1(1)		0.0
VMC (BCS+spiral) [38]				−0.532(1)		0.36
VMC (p-BCS) [16]	−0.442 991	−0.464 67	−0.478 40	−0.535 7(1)		0.0
FN [16]		−0.470 51	−0.485 21	−0.539 89(3)		0.162 5(30)
FNE [16]		−0.471 71	−0.486 91	−0.541 87(6)		0.176 5(35)
GFMCSR [39, 40]				−0.545(2)		0.205(10)
DMRG [41]						0.205(15)
QMC [42]					−0.669 437(5)	
series expansion [39][a]					−0.669 6(3)	
series expansion [43][a]				−0.550 2(4)		0.19(2)
LSW [16, 39][a]				−0.538(2)		0.238 7
1/S expansion [44][a]						0.266
1/S expansion [45][a]				−0.546 8		0.249 74
SBMFT [46][a]				−0.569 7		0.275
MSW (present study)[a]	−0.464 7	−0.463 9	−0.477 5	−0.530 3	−0.669 9	0.342 6

[a]These methods do not provide a rigorous upper bound for the ground-state energy.

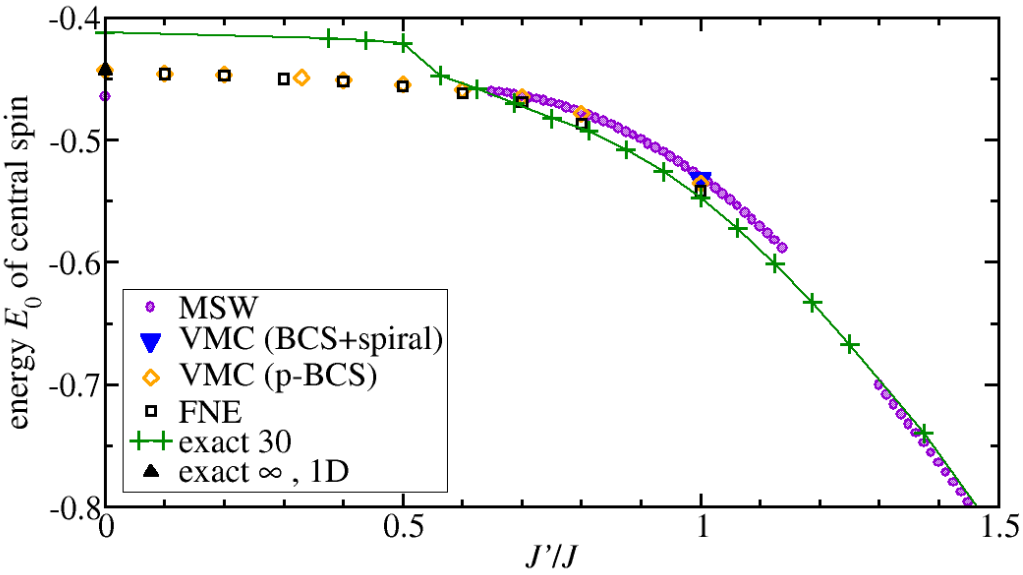

Figure 3. MSW results for the ground-state energy lie close to results from previous studies. Shown are the data of [16] for their VMC ansatz with a projected BCS wave function (p-BCS) and the improved FN effective Hamiltonian method (FNE). We further display the value obtained in the isotropic limit by [38] by use of a VMC method with a mixture of a BCS and a spiral-ordered wave function (BCS+spiral), and the exact result of the 1D limit. The numbers in the labels of the curves are the respective system sizes considered.

2.1.3. Order parameter and spin stiffness from the MSW theory. Our next step is to determine the regions where the presence of a finite order parameter M_0 and spin stiffness Υ reveal magnetic LRO. Even when M_0 and Υ are finite, a caveat is still in order: a finite order parameter with a very small stiffness might suggest that taking quantum fluctuations more completely into account than in the MSW theory could lead to a completely disordered state.

The order parameter M_0, drawn in figure 4, shows that magnetic LRO is present in the intervals $0.65 < \alpha < 1.14$ and $\alpha > 1.3$. This is to be contrasted with linear SW (LSW) theory, which predicts the breakdown of magnetic order only for $\alpha \lesssim 0.3$ [47].

In the isotropic case, $\alpha = 1$; however, the MSW order parameter is considerably higher than what is predicted by the LSW theory. Comparing to the best numerical estimates, which are presented in table 1, shows that in this respect the MSW theory performs worse than other analytical methods, such as Schwinger-boson mean-field theory (SBMFT) [46] or $1/S$ expansion [44, 45]. Nonetheless, we note that, among all analytical predictions, surprisingly LSW gives the one which is closest to the most recent numerical estimates. This strongly suggests that an adequate account of quantum corrections to the magnetization is a hard task for theories accounting for spin–wave interactions at a perturbative or mean-field level, and that non-perturbative approaches or approaches beyond mean-field theory would be necessary.

In the square lattice limit, $\alpha \to \infty$, on the other hand, both the MSW and LSW theories attain a staggered magnetization of 0.303, which compares favorably with the most recent estimates $M_0 = 0.30743(1)$ from quantum Monte Carlo calculations [48]. The MSW order

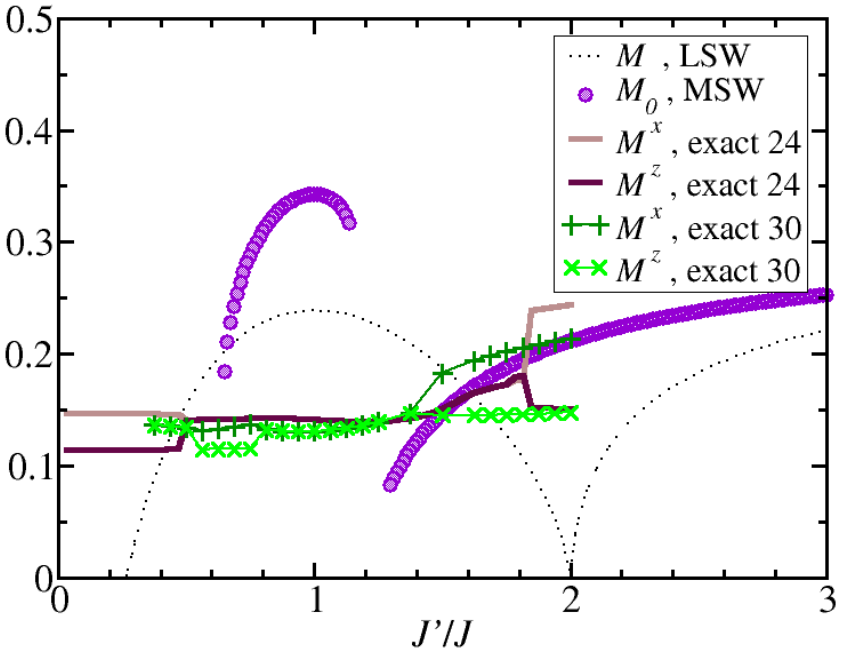

Figure 4. M_0 from the MSW theory compared with the LSW values and ED results (see section 2.1.5). The numbers in the labels of the curves are the respective system sizes considered in the calculations.

parameter drops drastically on approaching the region $1.14 \lesssim \alpha \lesssim 1.3$ and when reaching the region $\alpha \lesssim 0.65$ from above, the regions where the self-consistent description breaks down, further corroborating the assumption that in these regions magnetic LRO disappears in the true quantum ground state. This assumption is strongly reinforced by considering the Gaussian spin stiffness (figure 5): it vanishes at $\alpha = 0.65$ and it drops significantly when approaching $\alpha = 1.14$ from below.

There are various special cases of the SATL for which the spin stiffness has been calculated previously. In the square lattice limit, $\alpha \to \infty$, the MSW theory gives $\rho_\parallel/\alpha = 0.216$, somewhat overestimating the value from QMC $\rho_\parallel/\alpha = 0.175(2)$ [42]. In the isotropic triangular lattice, $\alpha = 1$, the spin stiffness from the MSW approach is $\rho_\parallel/\alpha = 0.113$. This value falls between the LSW spin stiffness $\rho_\parallel/\alpha = 0.122$ ([49]) and the estimate obtained from ED calculations after finite-size extrapolation, $\rho_\parallel/\alpha = 0.075$ [49]. The large-S expansion result, $\rho_\parallel/\alpha = 0.070$ [44], is closer to the ED result than the MSW value. In the limit of decoupled chains, $\alpha = 0$, the MSW theory achieves convergence (which was lost in the interval $0 < \alpha < 0.65$) and provides a spin stiffness $\rho_{xx}/\alpha = 0.309$ in the thermodynamic limit, relatively close to the exact result in the thermodynamic limit, $\rho_{xx}/\alpha = 1/4$ [50].

2.1.4. Spin and chirality correlations from the MSW theory. Now we describe the ordered phases found by the MSW ansatz for the Heisenberg SATL in more detail. To this end, we analyze the following quantities:

1. The ordering vector $\boldsymbol{Q}$ (figure 6; also see equation (A.9)). Three limiting values for the ordering vector are known. For $\alpha = 0$ intra-chain antiferromagnetic (Néel) order is

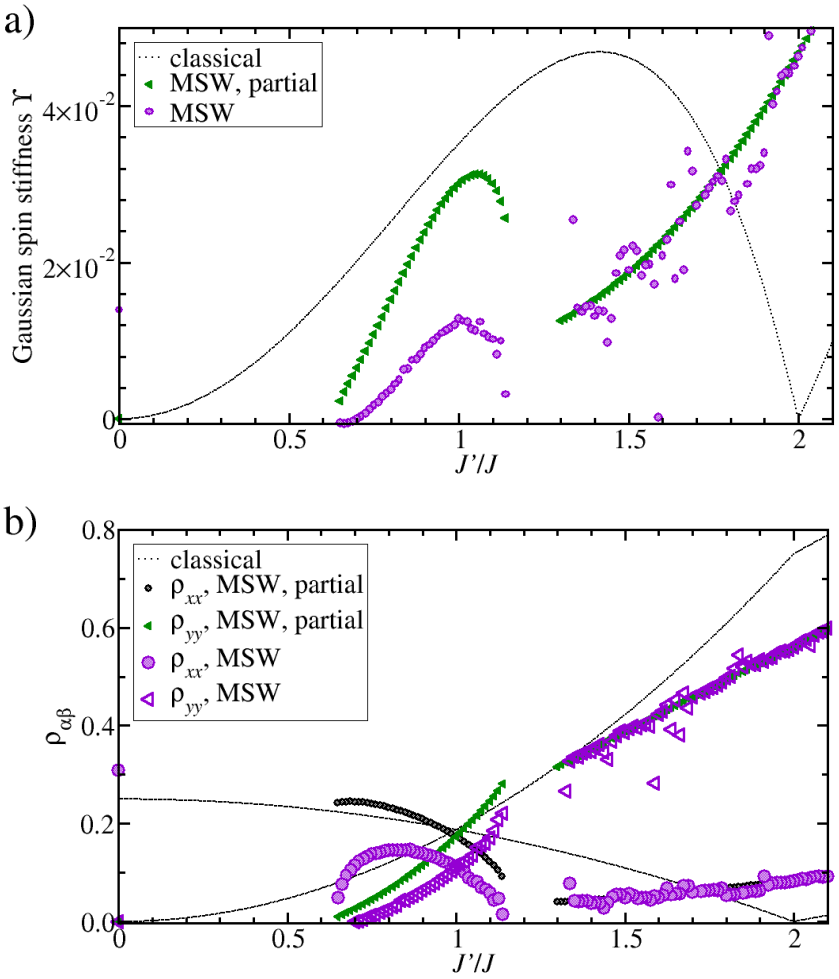

Figure 5. (a) The Gaussian spin stiffness Υ vanishes at $\alpha = 0.65$ and it drops significantly when approaching $\alpha = 1.14$ from below. (b) The components of the spin stiffness tensor. ρ_{yy} vanishes at $\alpha = 0$ and when reaching $\alpha = 0.65$ from above. ρ_{xx} decreases strongly when approaching $\alpha = 0.65^{+}$ and $\alpha = 1.14^{-}$, suggesting the onset of gapped spin-liquid phases. The mixed second derivative ρ_{xy} vanishes for symmetry reasons. The curves labeled 'partial' were obtained by application of equation (A.10).

described by $\boldsymbol{Q} = \pi\hat{x}$. For $\alpha \to \infty$ square-lattice Néel order is described by $\boldsymbol{Q} = 2\pi\hat{x}$. In the isotropic lattice ($\alpha = 1$), the threefold symmetry forces the ordering vector to $\boldsymbol{Q} = \frac{4\pi}{3}\hat{x}$;

2. The spin–spin correlations (figure 7). We analyze the spin–spin correlations of NNs through the two-site total spin,

$$T_{ij} \equiv \tfrac{1}{2}\langle(\boldsymbol{S}_i + \boldsymbol{S}_j)^2\rangle = \langle \boldsymbol{S}_i \cdot \boldsymbol{S}_j\rangle + \tfrac{3}{4}. \tag{2}$$

This quantity disappears if the spins are in a singlet, which is equivalent to perfect anticorrelation, takes the value $\frac{3}{4}$ if they are uncorrelated and the value 1 if the spins form a triplet, which means perfect correlation;

3. The mean-chiral correlations (figure 8). Spiral phases carry not only a magnetic order parameter, but also a chiral order parameter. In particular, a vector chirality can be

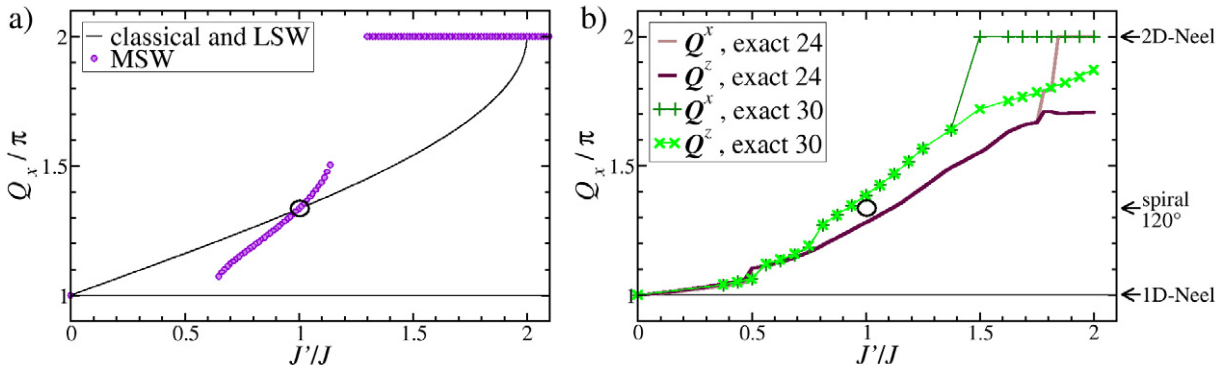

Figure 6. (a) The ordering wave-vector, Q_x, from MSW theory (equation (A.9)) shows a considerable shift with respect to the the classical and the LSW results. The black circle marks the order vector $Q_x = 120^\circ$ of the isotropic triangular lattice that is attained at $\alpha = 1$. (b) For ED, Q_x depends strongly on whether it is derived from M^x or from M^z. Also, the difference between the 24 and the 30 site cluster is significant. The numbers in the labels give the system sizes.

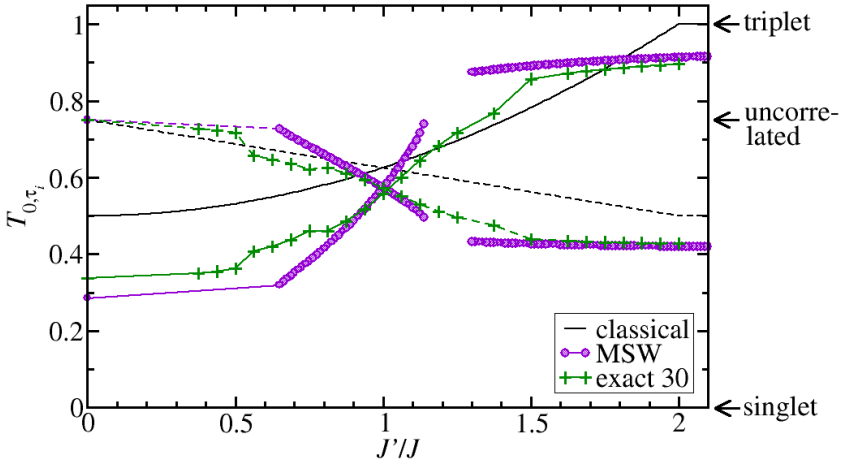

Figure 7. MSW and ED results show similar behavior of $T_{0,\boldsymbol{\tau}_i}$, with $\boldsymbol{\tau}_i = \boldsymbol{\tau}_1 \equiv (1, 0)$ (solid lines) and $\boldsymbol{\tau}_i = \boldsymbol{\tau}_2 \equiv (1/2, \sqrt{3}/2)$ (dashed lines), respectively. The numbers in the labels give the system sizes.

defined on an upward-pointing triangle with counter-clockwise labeled corners (i, j, k) as [51] $\kappa_\Delta = \frac{2}{3\sqrt{3}}[\boldsymbol{S}_i \times \boldsymbol{S}_j + \boldsymbol{S}_j \times \boldsymbol{S}_k + \boldsymbol{S}_k \times \boldsymbol{S}_i]_z$, and on a downwards pointing triangle with counter-clockwise labeled corners (i, l, j) as $\kappa_\nabla = \frac{2}{3\sqrt{3}}[\boldsymbol{S}_i \times \boldsymbol{S}_l + \boldsymbol{S}_l \times \boldsymbol{S}_j + \boldsymbol{S}_j \times \boldsymbol{S}_i]_z$. Chirality correlations are defined as [52]

$$\psi_- = \langle (\kappa_\Delta - \kappa_\nabla)\,(\kappa_{\Delta'} - \kappa_{\nabla'}) \rangle, \tag{3}$$

where the triangle pairs (Δ, ∇) and (Δ', ∇') share a $\boldsymbol{\tau}_1 \equiv (1, 0)$ edge. In figure 8, we plot the average chirality correlation of the central plaquette with all other plaquettes, normalized to the theoretical maximum 4/9. The MSW data have been obtained by expanding the chiral correlation up to the fourth order in the boson operators, which is

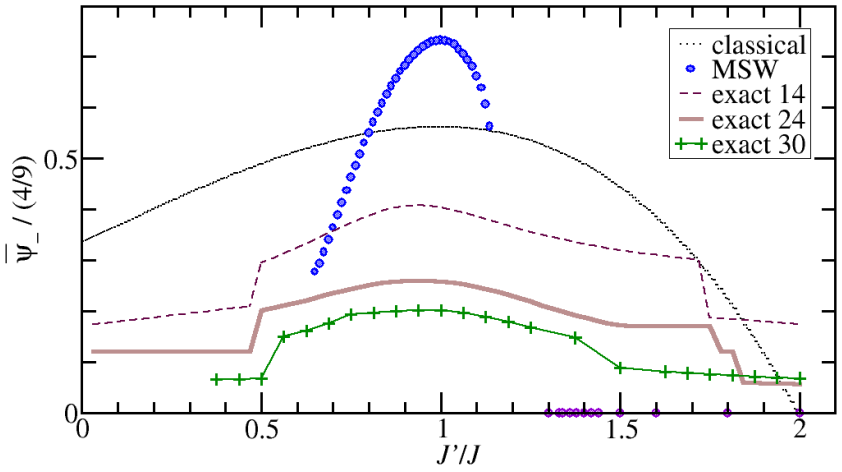

Figure 8. Comparison of the MSW and ED results for the mean chiral correlation normalized to the theoretical maximum of 4/9. The numbers in the labels give the system sizes.

consistent with the truncation of the bosonic Hamiltonian equation (A.1) to the same order. Including higher orders does not change the outcome in the regions where M_0 is large, but can yield different results where M_0 is small.

A comparison of these quantities shows a spiral phase at around $0.65 \lesssim \alpha \lesssim 1.14$ and a 2D-Néel-ordered phase for $\alpha \gtrsim 1.3$. Moreover, when approaching $\alpha \approx 0.65$ from above, the ordering vector, the spin–spin correlations and the ground-state energy approach their respective 1D values. This is an indication that below $\alpha \approx 0.65$ the true ground state of the system may enter a 1D-like spin-liquid phase. Nonetheless, the vanishing of the spin stiffness for $\alpha \to 0.65^+$ is not consistent with the onset of a *gapless* 1D spin-liquid phase, for which the spin stiffness should remain finite. Hence, the MSW results rather suggest that the phase appearing below $\alpha = 0.65$ is a *gapped* spin liquid, and that the gapless 1D spin-liquid phase, connected continuously with the limit $\alpha = 0$, is only attained for even smaller α. This seems consistent with the prediction of [16] that a gapped spin-liquid phase separates the spirally ordered phase from the 1D-like gapless disordered one.

2.1.5. Order parameter and correlations in comparison with exact diagonalization. In the case of ED, the static structure factor

$$S^{\alpha}(\boldsymbol{k}) = \frac{1}{N^2}\sum_{i,j}\langle S_i^{\alpha} S_j^{\alpha}\rangle \mathrm{e}^{-\mathrm{i}\boldsymbol{k}\cdot\boldsymbol{r}_{ij}} \quad (\alpha = x, y, z) \tag{4}$$

allows us to extract the order parameter M^{α}, which is defined as $M^{\alpha} = \sqrt{S^{\alpha}(\boldsymbol{Q})}$, where $\boldsymbol{Q}$ is the ordering vector associated with a peak in $S^{\alpha}(\boldsymbol{k})$. In the thermodynamic limit, this is equivalent to M_0 from the MSW theory. A comparison of both quantities can be found in figure 4. We plot both M^x and M^z due to the anisotropy caused by the triplet physics mentioned at the beginning of this section. Discontinuous jumps in the ED magnetizations are due to the change of the spin sector hosting the ground state, going from the singlet sector (characterized by $M^x = M^z$) to the triplet sector (characterized by $M^x \neq M^z$). We observe very severe deviations between the

ED data on the one side and the predictions from LSW and MSW theories on the other side: in particular, apart from the deviations between M^x and M^z, the ED data appear to be almost constant over a large α interval. The strong difference between ED results on the one hand and MSW/LSW predictions on the other can also be attributed to very significant finite-size corrections to the ED data—finite-size effects are particularly pronounced here, due to the open boundary conditions of ED clusters. Nonetheless, for $\alpha = 1$ the magnetization of the 30-site cluster gives $M^x = M^z \approx 0.13$, lying close to recent Monte Carlo estimates [21].

From the location of the peak of the structure factor one can extract the vector of predominant ordering, $\boldsymbol{Q}$, the x-component of which is plotted in figure 6. For MSW theory, we observe a significant shift with respect to the classical and LSW results (figure 6(a)). Remarkably, for the ED of the 30-site cluster, the $\boldsymbol{Q}$ corresponding to M^x (labeled as $\boldsymbol{Q}^x$ in the figure) indicates a transition from spiral to Néel order at around $\alpha \approx 1.4$, which lies well below the classical threshold $\alpha = 2$ (figure 6(b)). In contrast, the $\boldsymbol{Q}$ corresponding to M^z (labeled as $\boldsymbol{Q}^z$) increases smoothly up to $\alpha \approx 2$, where it undergoes a discontinuous transition to the square-lattice Néel value as well. However, increasing the system size from 24 to 30 spins shifts significantly the curves of $\boldsymbol{Q}^x$ and $\boldsymbol{Q}^z$ to the left, suggesting that for even larger sizes both curves might exhibit a discontinuous transition to the Néel-ordering vector for a value of α close to the transition indicated by MSW theory, $\alpha \approx 1.3$. Finally, we note that at $\alpha = 1$ the ED results deviate from the isotropic value $Q_x = 120^\circ$ because the required threefold symmetry is broken by the shape of the simulation cluster, figure 2.

The NN spin–spin correlations T_{ij}, equation (2),[7] are in qualitative agreement with the MSW results as well (figure 7). In particular, they exhibit 1D-like behavior at small α, a spiral phase in an intermediate parameter range around the isotropic limit $\alpha = 1$ and a 2D-Néel structure at large α.

Finally, we focus on the chirality correlations. Comparing such correlations for the 14, 24 and 30 spin clusters shows that they are strongly suppressed for $\alpha \lesssim 0.5$ and for $\alpha \gtrsim 1.4$, when going to larger lattice sites. This indicates that a non-spiral phase appears in this region in the thermodynamic limit, in agreement with our MSW calculations. The persistence of significant correlations in the region $0.5 \lesssim \alpha \lesssim 1.4$ indicates that spiral order in the ground state might persist in a portion of this parameter range.

In summary, despite the significant deviations in the magnitude of the order parameter, both ED and MSW theories give a coherent picture, both qualitatively and quantitatively, of the evolution of the nature of spin–spin correlations on increasing the α parameter, going from quasi-1D to spiral to Néel.

2.2. Discussion

Despite its limitations, the MSW approach with ordering vector optimization reproduces faithfully the main characteristics of the phase diagram as sketched in figure 1(b), and thus remarkably improves on the results that were previously obtained for this model with conventional spin-wave theories. A breakdown of magnetic order—along with a variety of observables such as the ordering vector or NN spin–spin correlations—indicates that a 1D-like spin liquid might be attained below $\alpha \approx 0.65$. Due to the partial account of quantum fluctuations provided by MSW theory, we can safely take this as a lower bound for a spin liquid in the true ground state. Furthermore, we find a relatively small region with spiral LRO between

[7] For ED we report the values of T_{ij} averaged over the central spins, where boundary effects are minimal.

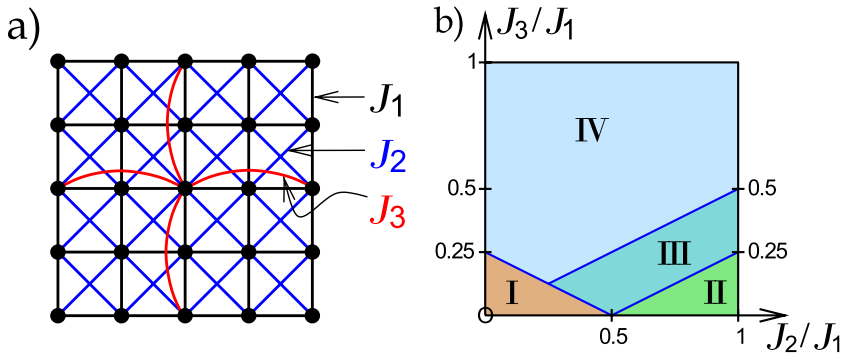

Figure 9. (a) A detail of the geometry of the $J_1J_2J_3$ model on a square lattice. NNs are coupled with bonds of strength J_1 (black), NNNs (along the diagonals) with J_2 (blue) and NNNNs with J_3 (red). (b) The classical phase diagram of the $J_1J_2J_3$ model shows four ordered phases. Phase I is characterized by Néel order on the square lattice. In phase II, the system decouples into two independently Néel-ordered sublattices with a doubled unit cell each. Phases III and IV are spirally ordered with $\boldsymbol{Q} = (q, \pi)$ and $\boldsymbol{Q} = (q, q)$, respectively.

$0.65 \lesssim \alpha \lesssim 1.14$. For $\alpha \gtrsim 1.30$ the system is ordered at the 2D-Néel wave-vector. Between $1.14 \lesssim \alpha \lesssim 1.30$ the breakdown of convergence suggests another candidate region for spin-liquid behavior.

3. The modified spin-wave theory on the J_1 J_2 J_3 model

In this section, we investigate another paradigmatic frustrated spin model, the $J_1J_2J_3$ model on the square lattice. It involves couplings between nearest neighbors (NN), J_1, next-nearest neighbours (NNN), J_2, and next-next-nearest neighbours (NNNN), J_3. A sketch of the geometry of the system may be found in figure 9(a). This model allows us to continuously tune the Hamiltonian from an unfrustrated antiferromagnetic square lattice to a highly frustrated magnet.

3.1. Classical and quantum mechanical phase diagram of the $J_1J_2J_3$ model at $T = 0$

The classical phase diagram of the $J_1J_2J_3$ model [34], [53–55] is sketched in figure 9(b). One identifies:

(I) A 2D-Néel phase with $\boldsymbol{Q} = (\pi, \pi)$ just as in the unfrustrated square lattice. It is delimited by the classical critical line $(J_2 + 2J_3)/J_1 = 1/2$;

(II) A phase where the system decouples into two independent J_2-sublattices with a doubled unit cell. Both are Néel-ordered individually. This phase is infinitely degenerate because the two sublattices can be rotated one with respect to the other without affecting the energy;

(III) A spiral phase with ordering vector $\boldsymbol{Q} = (q, \pi)$, where q varies continuously over the phase diagram;

(IV) A second spiral phase, this time with ordering vector $\boldsymbol{Q} = (q, q)$; $q \to \pi/2$ for $J_3 \to \infty$, attaining the limit of two decoupled and Néel-ordered J_3-sublattices.

This phase diagram is believed to change considerably in the quantum limit [27], [32–34]: in phase II, quantum fluctuations select the columnar-ordered states with $\boldsymbol{Q} = (\pi, 0)$ or $\boldsymbol{Q} = (0, \pi)$ from all the possible classical states. Furthermore, the Néel phase I increases in size considerably and Néel order persists up to the vicinity of the line $(J_2 + J_3)/J_1 = 1/2$. In the vicinity of this line, the classical order is believed to be destabilized and to be replaced by a non-magnetic state. The controversy about the exact nature of the ground state in this highly frustrated region, however, is still not settled. In particular, it has been suggested that it could have the nature of a *columnar valence bond crystal* [56] with both translational and rotational broken symmetries, of a *plaquette state* with no broken rotational symmetry [27] or of a *spin liquid* with all symmetries restored [57–61].

In the following, we investigate the quantum model using the MSW formalism, and compare it with recent results from PEPSs calculations. The MSW lattice size is $N = 32 \times 32$. In most of the $J_1 J_2 J_3$ parameter space, a lattice of this size is essentially already converged to the infinite lattice, except close to a quantum critical point.

In [62], some of us reported numerical calculations of the $J_1 J_2 J_3$ model based on the PEPS variational ansatz for varying lattice sizes. In the following, we will focus on the extrapolations to the thermodynamic limit, except if stated otherwise.

We first discuss in more detail the special cases of the $J_1 J_2$ model (i.e. $J_3 = 0$) and the $J_1 J_3$ model (i.e. $J_2 = 0$). Both models have been studied before within the MSW formalism [30], [63–68]. On the one hand, we confirm existing results on the $J_1 J_2$ case, for which the optimization of the ordering wave-vector returns only two possible values (corresponding to Néel order [$\boldsymbol{Q} = (\pi, \pi)$] or columnar order [$\boldsymbol{Q} = (\pi, 0)$ or $\boldsymbol{Q} = (0, \pi)$]), and we give further insight into the spin stiffness and the dimer–dimer correlation functions. On the other hand, we analyze the $J_1 J_3$ model with optimization of the ordering wave-vector, which proves crucial to correctly capture the quantum effects on the classical spiraling phases appearing in this case [30]. Finally, we give an overview of the entire quantum ground-state phase diagram of the $J_1 J_2 J_3$ model.

3.2. Ground-state properties of the $J_1 J_2$ model

Figures 10 and 11 report the results for the $J_1 J_2$ model from the MSW method as well as from PEPS calculations. For comparison, we also plot the values for the energy and magnetization that were obtained in [37] from diagonalization of small clusters. In agreement with other methods, e.g. exact diagonalization (ED) [37, 69, 70] or Schwinger-bosons [71], the MSW theory finds Néel order with $\boldsymbol{Q} = (\pi, \pi)$ at small J_2/J_1 and columnar order with $\boldsymbol{Q} = (\pi, 0)$ or $\boldsymbol{Q} = (0, \pi)$ at large J_2/J_1 (see figure 10). As it is well known from previous studies, there is a region between $0.56 \lesssim J_2/J_1 \lesssim 0.62$ where the 2D-Néel-ordered and the columnar state are both stable solutions within the MSW theory. The starting point of the self-consistent calculations determines which type of order is returned as the solution. However, the solutions differ in energy and therefore one of them is only a local free energy minimum of the self-consistent equations. The transition from 2D-Néel order to columnar order takes place at $J_2/J_1 \simeq 0.6$. For the PEPS results, we extract the wave-vector of dominant spin correlations $\boldsymbol{Q}^{\mathrm{PEPS}}$ from the location of the peak of the static structure factor,

$$M(\boldsymbol{k}) = \sqrt{\frac{1}{N^2} \sum_{ij} \langle \boldsymbol{S}_i \cdot \boldsymbol{S}_j \rangle \mathrm{e}^{-\mathrm{i}\boldsymbol{k}\cdot\boldsymbol{r}_{ij}}}. \tag{5}$$

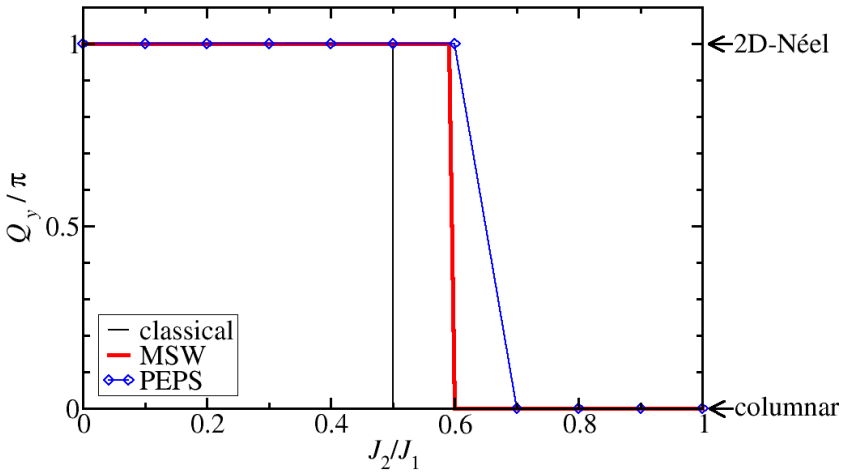

Figure 10. For the $J_1 J_2$ model, the y-component of the ordering vector shows a considerable shift in the quantum model with respect to the classical value.

In agreement with the MSW prediction, $\boldsymbol{Q}^{\mathrm{PEPS}}$ is located at the Néel value (π, π) up to $J_2/J_1 = 0.6$, while above this it lies at the value of columnar order $(\pi, 0)$.

We find a remarkable correspondence of the ground-state energy per spin between the MSW prediction and ED results extrapolated to the infinite lattice from [37] (figure 11(a)). Moreover, the noticeable kink associated with the Néel-to-columnar transition of MSW theory at $J_2/J_1 = 0.6$ is exhibited as well by the 40-sites system from [37]. Therefore, ED confirms that $J_2/J_1 = 0.6$ marks a transition point, although in the true ground state such a transition might connect the columnar state to a quantum-disordered state. Similarly good agreement is found with the PEPS results extrapolated to the infinite-size limit.

As shown in figure 11(b), at small J_2/J_1, i.e. deep in the Néel phase, the finite-size extrapolation of the ED-staggered magnetization from [37] lies very close to the MSW results. As is well known [29], in the unfrustrated square lattice limit ($J_2 = 0$) the MSW value $M_0 = 0.303$ is only slightly smaller than QMC results, for which the most recent estimates give $M_0 = 0.307\,43(1)$ [48]. For the PEPS calculations an analogous quantity can—similar to section 2.1.5—be derived from the peak height of the static structure factor, equation (5). We show its finite-size extrapolation in figure 11(b). In the Néel phase PEPS agrees very well with the MSW theory, considerably better than ED, which decreases faster toward the strongly frustrated region. In the entire columnar phase, however, PEPS and ED data lie closer together, while MSW overestimates the order parameter. Around the transition, however, agreement between PEPS and MSW theory is very good. The PEPS data suggest that the magnetically disordered region, predicted by ED to occur in the range $0.35 \lesssim J_2/J_1 \lesssim 0.66$, is either much smaller or does not occur at all.

The MSW spin stiffness $\rho_{\parallel} \equiv (\rho_{xx} + \rho_{yy})/2$, however, while being finite for any considered value of the ratio J_2/J_1, is strongly suppressed in the region $0.3 \lesssim J_2/J_1 \lesssim 0.6$ (figures 11(c) and (d)), suggesting as usual that accounting for quantum fluctuations beyond the MSW approximation could lead to the disappearance of magnetic order. A suppression of spin stiffness is also observed in previous results coming from ED of finite clusters [69] or from the Schwinger-boson approach [71, 72]. As a consequence, even though the MSW admits a stable solution with magnetic order for any J_2/J_1 value, for $J_2/J_1 = 0.6$ it exhibits a clear transition

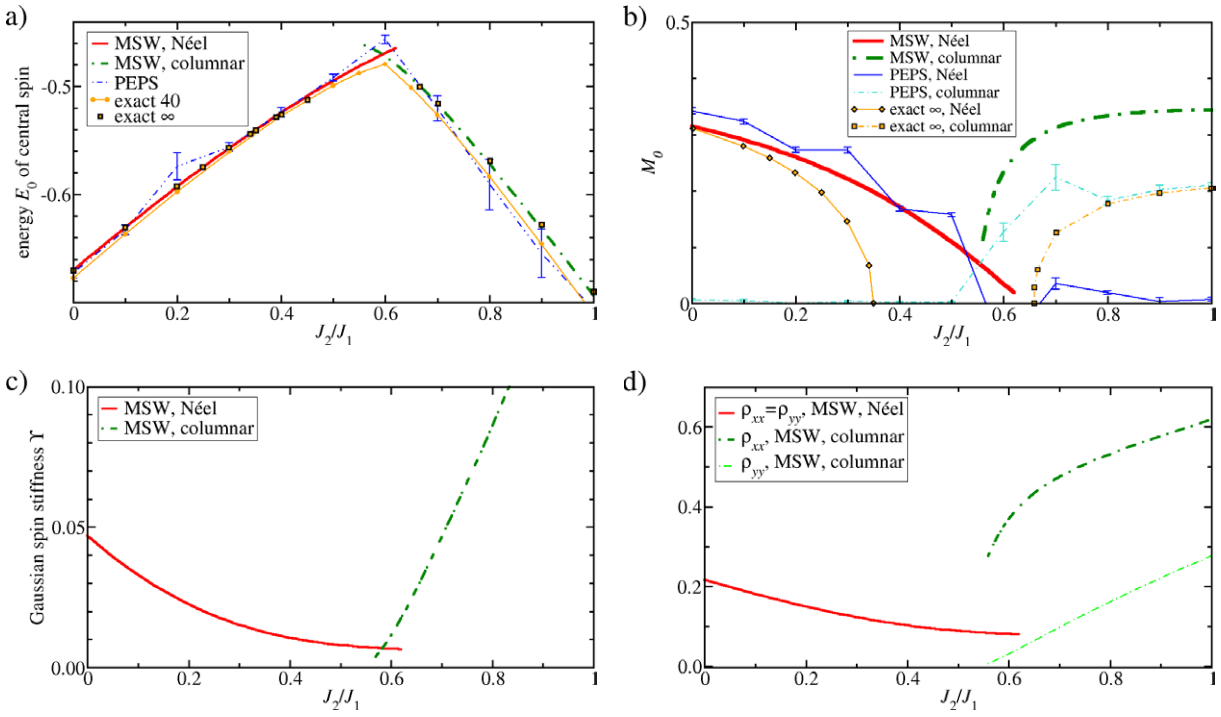

Figure 11. Comparison, for the J_1J_2 model, of MSW data to PEPS results extrapolated to the thermodynamic limit and ED from [37] [for the 40-spin cluster (labeled 'exact 40') and extrapolated to the thermodynamic limit ('exact ∞')]. For the MSW method, the curves obtained when starting the self-consistent iteration from a Néel state (thick red line) and from a columnar-ordered state (thick dot-dashed green line) are both included. The figures show (a) the ground-state energy of the central spin; (b) the MSW order parameter M_0 compared to $M(\pi, \pi)$ (Néel) and $M(\pi, 0)$ (columnar) derived from PEPS calculations; (c) the Gaussian spin stiffness and (d) components of the spin stiffness tensor. In the Néel phase $\rho_{xx} = \rho_{yy}$ by symmetry. The partial spin stiffnesses $\rho_{\alpha\beta}^{\text{partial}}$ are found to equal the total ones, $\rho_{\alpha\beta}$.

from *soft* Néel order to a *stiff* columnar order, suggesting that this transition could actually separate the columnar state from a quantum-disordered phase.

3.2.1. Dimer correlations in the J_1J_2 model. The nature of the state in the transition region between Néel and columnar order, where magnetic order is strongly reduced, can be further investigated through the study of the dimer–dimer correlations

$$C_{ijkl} = \langle (\boldsymbol{S}_i \cdot \boldsymbol{S}_j)\,(\boldsymbol{S}_k \cdot \boldsymbol{S}_l) \rangle, \tag{6}$$

where (i, j) and (k, l) are pairs of neighboring spins. Figure 12 sketches the expectation for the dimer–dimer correlations in (a) a columnar valence-bond crystal and (b) a columnar magnetic state.

In figure 13, we show the spatially resolved dimer–dimer correlations from MSW theory. Below $J_2/J_1 = 0.6$ the dimer–dimer correlations have a structure compatible with a Néel state

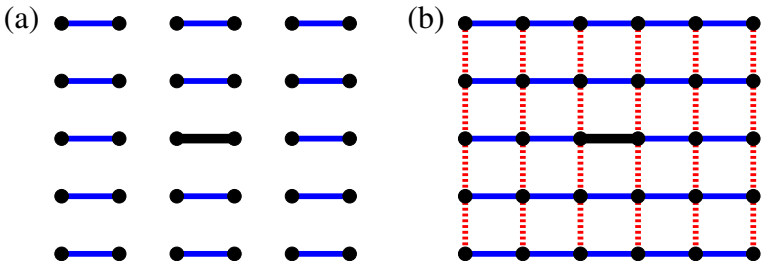

Figure 12. Sketch of dimer–dimer correlations in (a) a valence bond crystal and (b) a columnar state. Black dots are lattice sites. Blue solid (red dashed) lines are dimers correlated (anti-correlated) with the central dimer (thick black line).

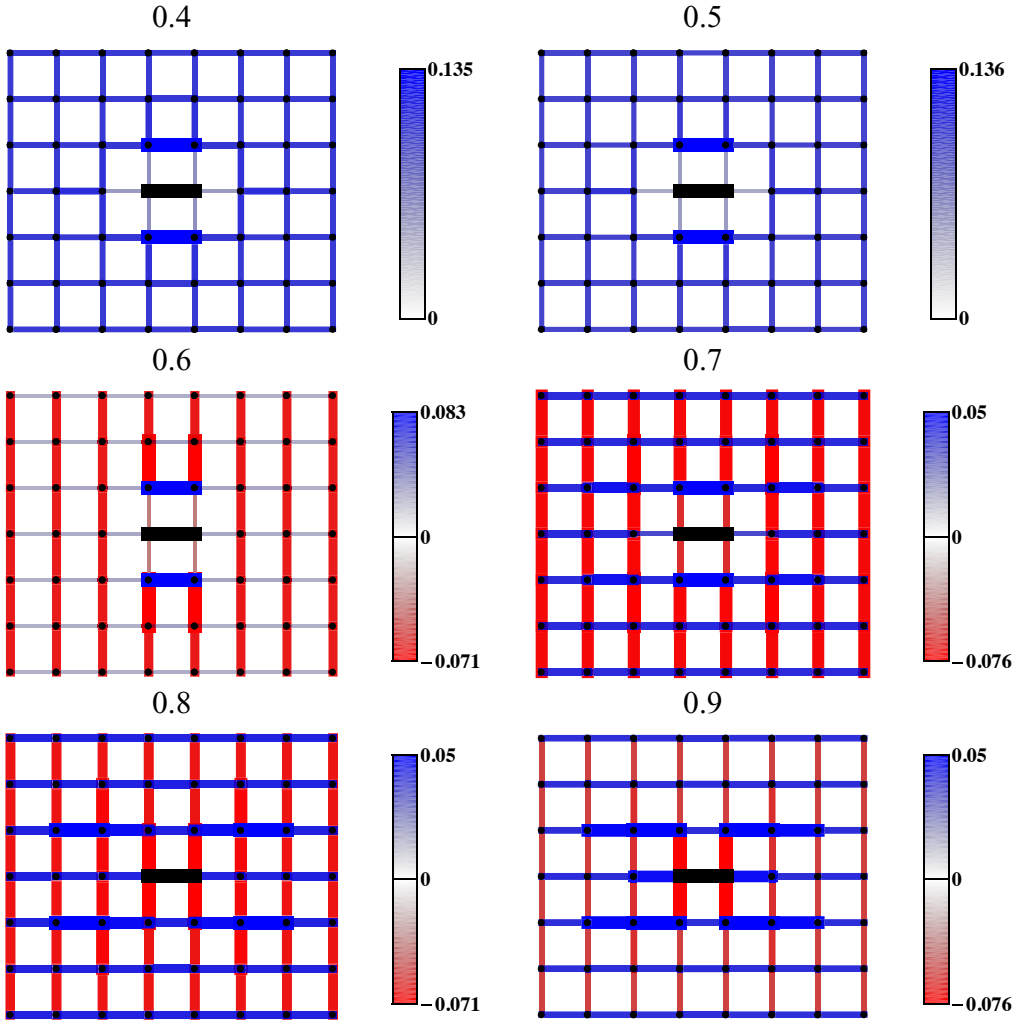

Figure 13. MSW correlations of the black central dimer with the other dimers of a 32×32 lattice (zoom on central region). The thickness of the lines is a nonlinear function of the absolute strength of the dimer correlations. Note the change of the maximum of the linear color scales for different values of J_2/J_1. Below $J_2/J_1 = 0.4$ and above $J_2/J_1 = 0.9$, the qualitative changes are minimal.

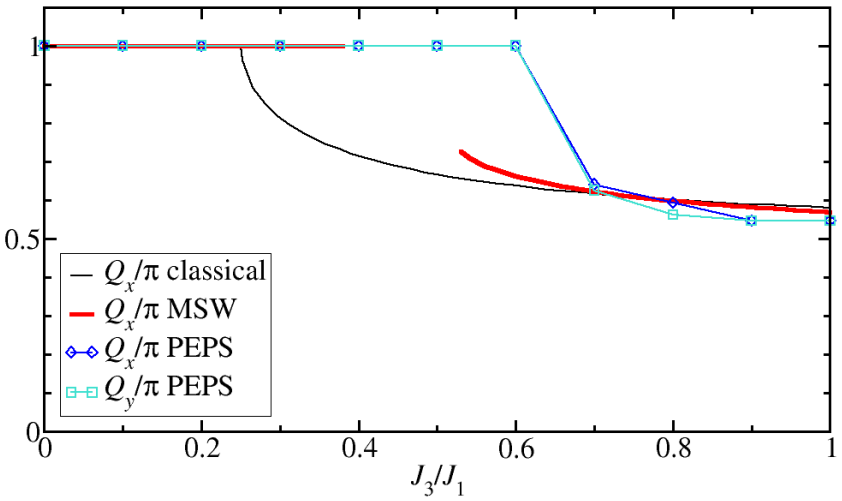

Figure 14. Position (Q_x, Q_y) of the peak of the structure factor for PEPS and the ordering vector $Q_x = Q_y$ of the MSW theory for the $J_1 J_3$ model. A comparison with the classical ordering vector $Q_x^{\mathrm{cl}} = Q_y^{\mathrm{cl}}$ shows that quantum fluctuations stabilize Néel order.

(namely they are positive and nearly equal for all bond pairs), while above $J_2/J_1 = 0.6$ the dimer–dimer correlations acquire the expected structure in a columnar state, with opposite signs for the correlations between dimers of the same spatial orientation (both horizontal and both vertical) and between dimers of opposite orientations. Nonetheless, for $J_2/J_1 \lesssim 0.7$, remarkably the MSW theory shows a short-range modulation in the strength of the dimer correlations whose structure is compatible with that of a valence-bond crystal. Although the MSW theory is not appropriate to characterize non-magnetic states such as a valence-bond crystal, it is remarkable to observe that it identifies a columnar valence-bond structure as the dominant form of dimer correlations at short range; this indication is consistent with, e.g. the results of PEPS [62], which also point toward columnar valence-bond order in the non-magnetic region of the $J_1 J_2$ model.

3.3. Ground-state properties of the $J_1 J_3$ model

We now turn to the $J_1 J_3$ model. Classically, this model has a transition from Néel to spiral order at $J_3 = 0.25 J_1$. Recent PEPS calculations show that for $S = 1/2$ Néel order persists up to approximately $J_3/J_1 = 0.3$ [62]. Above this point, the peak of the structure factor is still at the Néel-ordering vector (π, π) but its height vanishes in the thermodynamic limit, which suggests a complete loss of magnetic LRO. A different type of LRO arises anew at approximately $J_3/J_1 = 0.6$ with an ordering vector $\boldsymbol{Q} = (q, q)$ that tends to $(\pi/2, \pi/2)$ in the limit of large J_3 (see figure 14). For large-enough J_3 the nature of the ordered phase becomes similar to that of the classical limit.

The optimization of the ordering wave vector within MSW calculations shows that, for small J_3/J_1, Néel order persists up to $J_3/J_1 = 0.39$ (see figure 14), confirming the assumption that quantum fluctuations stabilize Néel order against spiral order with respect to the classical limit. Coming from the opposite limit of $J_3 \sim J_1$, we observe a spiral phase with continuously varying pitch vector $\boldsymbol{Q} = (q, q)$, where q approaches $\pi/2$ for $J_3/J_1 \to \infty$, and increases up to $q \approx 0.7\pi$ for $J_3/J_1 \to 0.52^+$. In the region $0.39 < J_3/J_1 < 0.52$, convergence of the MSW

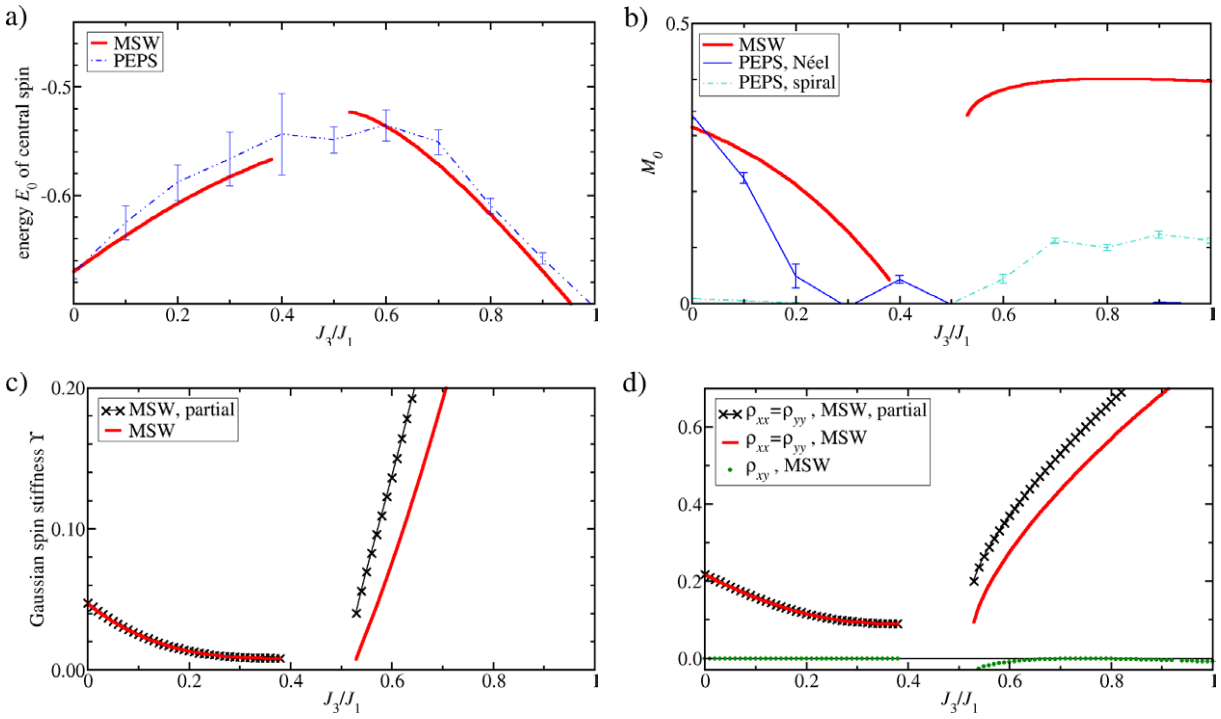

Figure 15. MSW and PEPS results on the $J_1 J_3$ model. Shown is (a) the energy per spin; (b) the order parameter M_0 for MSW theory and for PEPS the peak height of the structure factor at $\boldsymbol{Q} = (\pi, \pi)$ (Néel) and $\boldsymbol{Q} = (q, q)$ (spiral); (c) the Gaussian spin stiffness; (d) the components of the spin-stiffness tensor (where $\rho_{xx} = \rho_{yy}$ by symmetry, and $\rho_{xy}^{\text{partial}} \equiv 0$).

calculations breaks down, which points at a possible spin-liquid phase, in agreement with the predictions from PEPS calculations.

Figure 15 (a) shows the PEPS energy extrapolated to the thermodynamic limit. Agreement with the MSW results is again found to be extremely good.

The indication of a disordered phase drawn from the breakdown of the MSW theory is further corroborated by the order parameter M_0 (figure 15(b)), which decreases strongly for $J_3/J_1 \to 0.39^-$ and for $J_3/J_1 \to 0.52^+$, and by the spin stiffness (figure 15(c) and (d)), which is drastically reduced when approaching the above two limits. In particular, the Gaussian spin stiffness Υ is already strongly reduced for $J_3/J_1 \gtrsim 0.3$. These results are consistent with the vanishing of the spin stiffness at $J_3/J_1 = 0.35$ that was found by ED of a system of 20 sites in [73].

A destabilization of magnetic order at around $J_3/J_1 \gtrsim 0.3$ seems to be confirmed by the PEPS order parameter, figure 15(b), which vanishes in the range $0.3 \lesssim J_3/J_1 \lesssim 0.5$. Note that, again, we find that the PEPS order parameter deep in the Néel phase is similar to the MSW data, but that in the spiral phase MSW data for the order parameter lie well above the PEPS ones.

In our calculations, despite using the same equations as in [30], we find a considerably larger breakdown region. However, the region where our calculations do not yield a result is very stable, i.e. it does not depend much on system size nor on the exact algorithm for solving the self-consistent MSW equations.

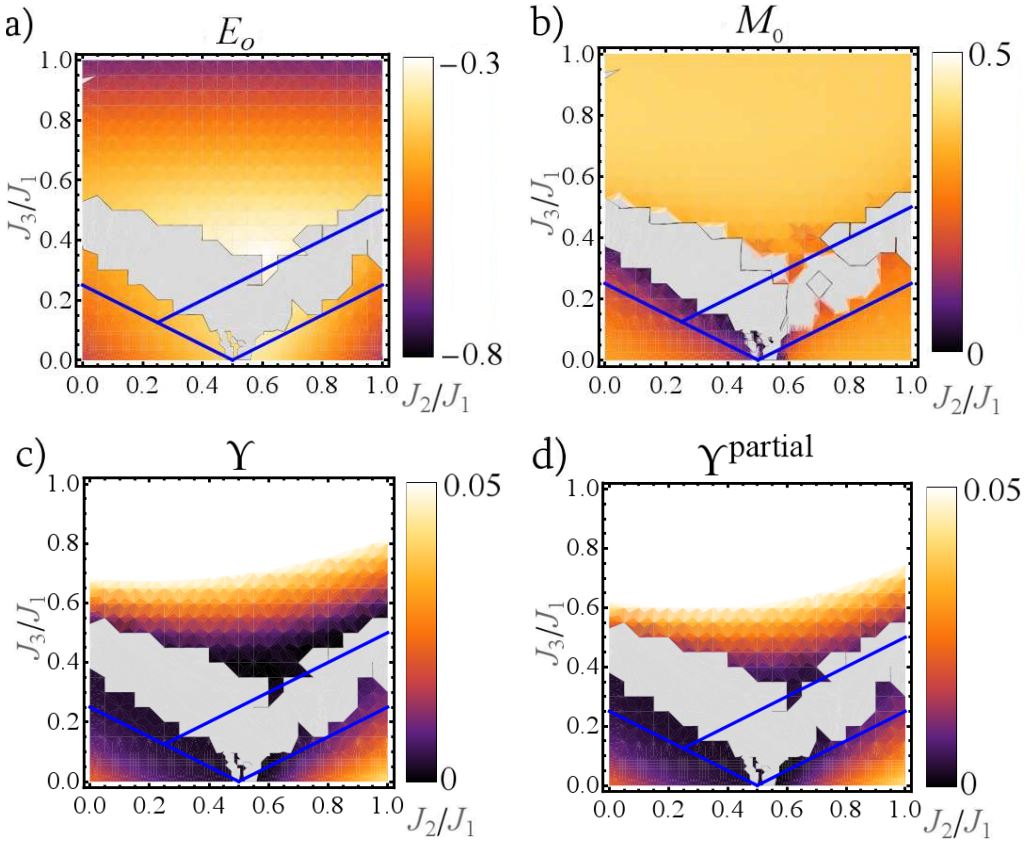

Figure 16. (a) Ground-state energy per spin E_0, (b) order parameter M_0, (c) Gaussian spin stiffness Υ and (d) Gaussian spin stiffness $\Upsilon^{\text{partial}}$ calculated via equation (A.10). Note that Υ and $\Upsilon^{\text{partial}}$ rise beyond the linear scale in the upper half of the plot. In the gray areas, convergence of the self-consistent equations could not be reached. The blue lines are the classical phase boundaries.

The precise nature of the state in the candidate region for quantum-disordered behavior cannot be determined reliably by the use of the MSW theory. From an analysis of the dimer–dimer correlations in the convergence regions, we can find no indications of any exotic disordered quantum state; on the contrary, PEPS results indicate a plaquette state in the region of maximal frustration $J_3 \approx J_1/2$ [62].

3.4. Ground-state phase diagram of the $J_1J_2J_3$ model

3.4.1. MSW results. After having investigated the two limiting cases of the J_1J_2 and the J_1J_3 models, we consider, more generally, the $J_1J_2J_3$ model over the relevant parameter range $0 \leqslant J_2/J_1, J_3/J_1 \leqslant 1$. As already seen in the case of the J_1J_3 model, we observe a sizable parameter range over which the convergence of MSW theory breaks down, and which is then pointed out as a candidate region for non-magnetic behavior. We note that, while convergence is achieved for any J_2/J_1 ratio at $J_3 = 0$, a region of convergence breakdown opens up by adding a small J_3 component around $J_2/J_1 \approx 0.5$. The energy per spin increases when approaching this region, showing the increased influence of frustration (figure 16(a)). The indications for a

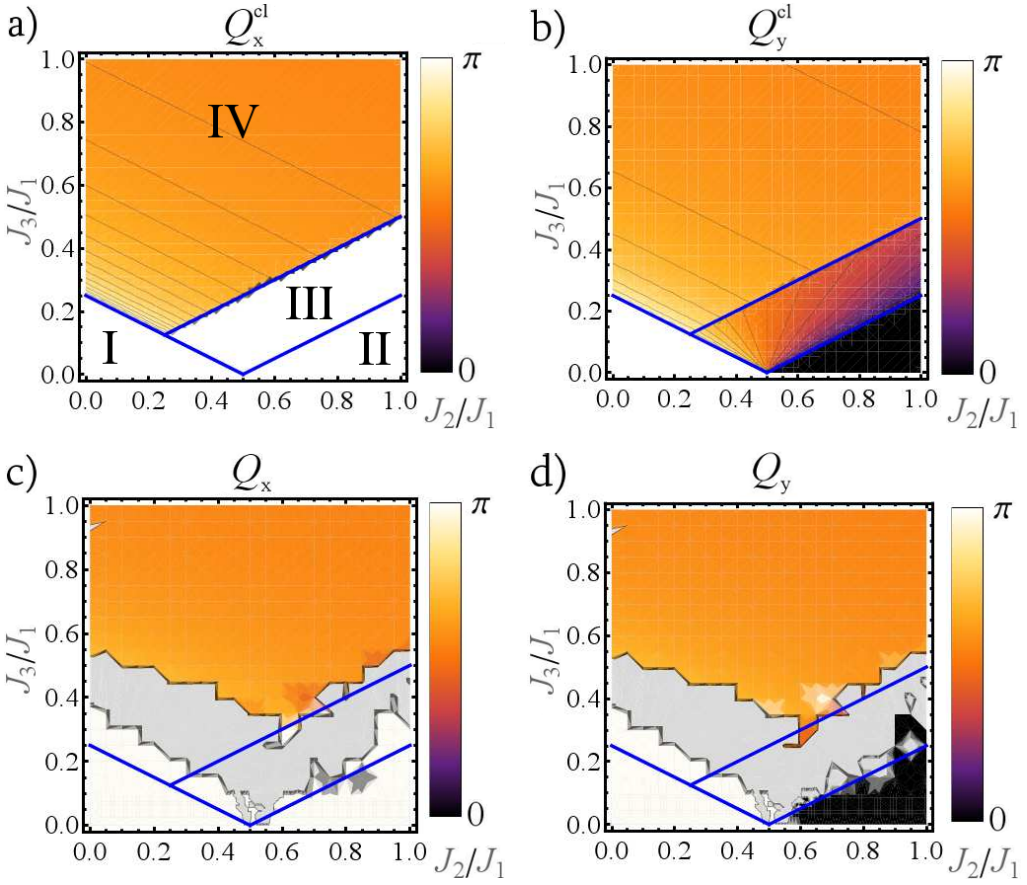

Figure 17. Ordering vector for the $J_1J_2J_3$ model in linear color scale. In the gray area, convergence of the self-consistent equations could not be reached. (a) x-component, and (b) y-component of the classical ordering vector; (c) x-component, and (d) y-component of the quantum mechanical MSW ordering vector. The blue lines are the classical phase boundaries, which divide (I) a Néel-ordered phase, (II) a phase with two independently Néel-ordered sublattices with a doubled unit cell each and spirally-ordered phases with (III) $Q = (q, \pi)$ and (IV) $Q = (q, q)$.

quantum-disordered phase in the breakdown region is corroborated by the decrease of the order parameter (figure 16(b)) and the spin stiffness (figures 16(c) and (d)) when approaching the breakdown region.

The nature of the phases where MSW reaches convergence can be seen in the ordering vector, which we display in figure 17 in comparison with the classical one. We find three ordered phases: (1) for small J_3/J_1 and J_2/J_1, we find a Néel-ordered phase. Its boundary is pushed upward to higher values of J_3/J_1 with respect to the classical limit; (2) a columnar phase is found at small J_3/J_1 but larger $J_2/J_1 \gtrsim 0.6$; (3) for large J_3/J_1 a spiral phase arises with an ordering vector $\boldsymbol{Q} = (q, q)$ that approaches $\boldsymbol{Q} = (\pi/2, \pi/2)$ for large J_3/J_1. As a consequence, a most dramatic effect of quantum fluctuations seems to be the disappearance of phase III in the classical phase diagram, characterized by magnetic order at a pitch vector $\boldsymbol{Q}_{cl} = (q, \pi)$ with continuously varying q, in favor of the columnar phase and of a potentially quantum-disordered phase.

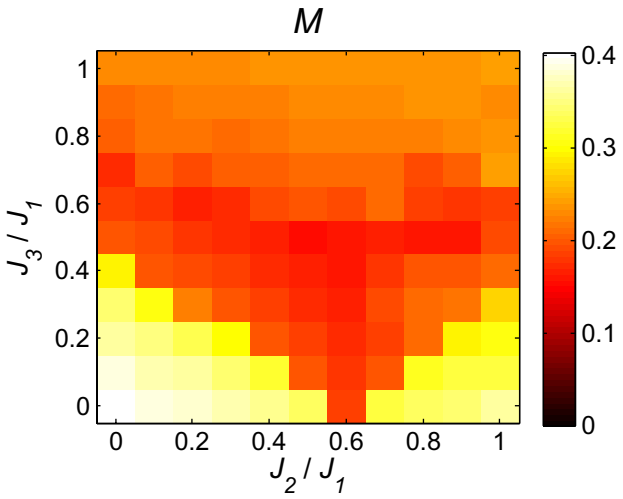

Figure 18. $M(Q)$ (equation (5)) for a PEPS calculation on an 8×8 lattice with auxiliary dimension $D = 3$. A low value marks the destabilization of magnetic LRO.

3.4.2. Comparison to PEPS calculations. In figure 18, we display the peak height of the static structure factor, equation (5), from a PEPS calculation on an 8×8 lattice with auxiliary dimension $D = 3$. We observe a broad asymmetric v-shaped region in which the magnetic order, quantified by the height of the peak in the structure factor, is strongly suppressed. We note that this region is strongly reminiscent of (albeit broader than) the breakdown region of the MSW theory. In particular, the asymmetry is due to the fact that the bottom of the 'v' lies at $J_2/J_1 > 0.5$, a characteristic which is shared with the MSW phase diagram. While a thorough finite-size scaling analysis of the PEPS data would be necessary to determine the precise boundaries of the possible magnetically disordered regions, quantitative information can be extracted even from the finite-size PEPS data concerning the location of the pitch vector of the dominant (long-ranged or short-ranged) magnetic correlations.

Similar to what happens in the above spin-wave calculations, a pronounced peak at the Néel-ordering vector (π, π) appears if both J_2/J_1 and J_3/J_1 are small, while at large J_2/J_1 but small J_3/J_1 the structure factor is peaked at the columnar-ordering vector $(\pi, 0)$. For large J_3/J_1, finally, the peak is located at (q, q), where q tends to $\pi/2$.

4. Conclusion

In this work, we made use of Takahashi's MSW theory with ordering vector optimization to determine the ground-state phase diagram of two paradigmatic models of 2D frustrated antiferromagnetism: the $S = 1/2$ Heisenberg model on the SATL and on the $J_1 J_2 J_3$ lattice. The optimization of the ordering vector shows dramatic quantum corrections to the ordering vector for spiraling states present in both models: such corrections show the general trend of promoting collinearly ordered states (either Néel or columnar states) against spiraling ones. Both for the triangular and the $J_1 J_2 J_3$ lattice, the MSW theory breaks down over a sizable region of parameter space, showing a dramatic suppression of the order parameter and of the spin stiffness as the breakdown region is approached: this finding is strongly suggestive

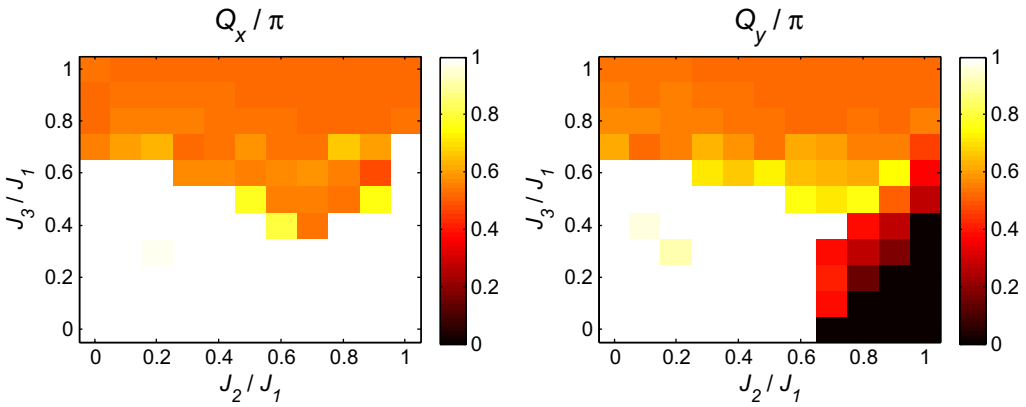

Figure 19. Components of the ordering vector for a PEPS calculation on an 8×8 lattice with auxiliary dimension $D = 3$.

of the appearance of quantum-disordered regions in the phase diagram of the models under investigation, an issue that is still under intense debate. The extent of the quantum-disordered regions estimated via the MSW theory generally appears to be lower than that estimated by more accurate numerical techniques that take into account quantum fluctuations in a more complete fashion. Hence, one can draw two main conclusions from our results: on the one hand, MSW might still converge to a magnetically ordered ground state even though the true ground state is disordered—although in this case it will probably feature a small value for the order parameter, or a small stiffness, suggesting that the magnetic order is not robust when dealing with quantum fluctuations more accurately; on the other hand, the breakdown of MSW theory seems to be a strong indication that the true ground state is disordered.

In particular, in the case of the SATL, MSW theory completely breaks down for sufficiently weak couplings between the chains composing the lattice, suggesting that the system remains in a disordered 1D-like state even when the chains are coupled, as already predicted by recent variational approaches. Another disordered phase appears when the inter-chain couplings exceed the intra-chain ones: this phase is sandwiched in between the spiral phase of the nearly isotropic triangular lattice and the Néel phase appearing at large inter-chain couplings. In the case of the $J_1 J_2 J_3$ lattice, a large breakdown region separates the Néel-ordered region for small J_2 and J_3, from the columnar-ordered region for $J_2 > J_1/2$ and small J_3, and from the spiral phase at large J_3. Hence, a general conclusion that we can draw from the study of these two models is that collinearly ordered phases (Néel and columnar) and spiral phases cannot be connected adiabatically—at least at the MSW level—but they are always separated by a breakdown region; this is a signal that in the true ground-state collinear and spiral phases might always be divided by an intermediate quantum-disordered phase.

Quantitative comparisons with more accurate methods (ED, and variational ansatze based on projected BCS states and PEPS) reveal that the MSW theory with ordering wave-vector optimization goes well beyond linear spin-wave theory in dealing with quantum effects, and it correctly accounts for the quantum correction to the ordering wave-vector of the ordered phases, and for the strong suppression (or total cancellation) of magnetic order in correspondence with the candidate regions for quantum-disordered behavior. Given its flexibility and its modest numerical cost, MSW theory therefore serves as a unique tool for the identification of novel quantum phases in strongly frustrated quantum Heisenberg antiferromagnets.

Acknowledgments

PH and TR acknowledge the hospitality of the Kavli Institute for Theoretical Physics, where this work was finalized. This research was supported in part by the National Science Foundation under grant no. PHY05-51164, the Caixa Manresa, Spanish MICINN (FIS2008-00784 and Consolider QOIT), EU Integrated Project AQUTE, the EU STREP NAMEQUAM, and ERC Advanced Grant QUAGATUA.

Appendix. Modified spin-wave formalism for Heisenberg antiferromagnets

In this appendix, we shortly review the MSW formalism as applied to Heisenberg antiferromagnets. The full description of the approach—as applied to XY models—can be found in [31].

The Dyson–Maleev transformation [74, 75] maps the Heisenberg Hamiltonian, equation (1), to the nonlinear bosonic Hamiltonian

$$\begin{aligned}\mathcal{H} = \frac{1}{4}\sum_{i,j} J_{ij}\Big\{&[2S(a_i^\dagger a_j + a_i a_j^\dagger) - a_i^\dagger a_j^\dagger a_j a_j - a_i^\dagger a_i a_i a_j^\dagger](1+\cos(\boldsymbol{Q}\cdot\boldsymbol{r}_{ij}))\\ &+[2S(a_i^\dagger a_j^\dagger + a_i a_j) - a_i a_j^\dagger a_j a_j - a_i^\dagger a_i a_i a_j](1-\cos(\boldsymbol{Q}\cdot\boldsymbol{r}_{ij}))\\ &+4[S^2 - S(a_i^\dagger a_i + a_j^\dagger a_j) + a_i^\dagger a_i a_j^\dagger a_j]\cos(\boldsymbol{Q}\cdot\boldsymbol{r}_{ij}) + \mathcal{O}\left(\frac{1}{S}\right)\Big\},\end{aligned} \tag{A.1}$$

where a_i ($a_i^\dagger$) destroys (creates) a Dyson–Maleev boson at site i, S is the length of the spin, and $\boldsymbol{Q}$ the ordering vector. Here, we neglected the kinematic constraint which restricts the Dyson–Maleev–boson density n to the physical subspace $n < 2S$, given by the length of the spins S. Moreover, we dropped terms with six boson operators, which are of order $\mathcal{O}[n/(2S)^3]$ and are negligible for $n/(2S) < 1$. Using Wick's theorem [76], and defining the correlators $\langle a_i^\dagger a_j\rangle = F(\boldsymbol{r}_{ij}) - \frac{1}{2}\delta_{ij}$ and $\langle a_i a_j\rangle = \langle a_i^\dagger a_j^\dagger\rangle = G(\boldsymbol{r}_{ij})$, the expectation value $E \equiv \langle\mathcal{H}\rangle$ can be written as

$$\begin{aligned}E = \frac{1}{2}\sum_{i,j} J_{ij}\Bigg\{&\left[S + \frac{1}{2} - F(0) + F(\boldsymbol{r}_{ij})\right]^2 (1+\cos(\boldsymbol{Q}\cdot\boldsymbol{r}_{ij}))\\ &-\left[S + \frac{1}{2} - F(0) + G\left(\boldsymbol{r}_{ij}\right)\right]^2 (1-\cos(\boldsymbol{Q}\cdot\boldsymbol{r}_{ij}))\Bigg\}.\end{aligned} \tag{A.2}$$

After Fourier transforming, $a_{\boldsymbol{k}} = \frac{1}{\sqrt{N}}\sum_i a_i e^{-i\boldsymbol{k}\cdot\boldsymbol{r}_i}$, where N is the number of sites, and a subsequent Bogoliubov transformation, $\alpha_{\boldsymbol{k}} = \cosh\theta_{\boldsymbol{k}}\, a_{\boldsymbol{k}} - \sinh\theta_{\boldsymbol{k}}\, a_{-\boldsymbol{k}}^\dagger$ and $\alpha_{-\boldsymbol{k}}^\dagger = -\sinh\theta_{\boldsymbol{k}}\, a_{\boldsymbol{k}} + \cosh\theta_{\boldsymbol{k}}\, a_{-\boldsymbol{k}}^\dagger$, we minimize the free energy under the constraint of vanishing magnetization at each site, $\langle a_i^\dagger a_i\rangle = S$ [29]. (This guarantees that the kinematic constraint is satisfied in the mean.) This yields a set of self-consistent equations,

$$\tanh 2\theta_{\boldsymbol{k}} = \frac{A_{\boldsymbol{k}}}{B_{\boldsymbol{k}}} \tag{A.3}$$

with

$$A_{\boldsymbol{k}} = \frac{1}{N}\sum_{i,j} J_{ij}(1-\cos(\boldsymbol{Q}\cdot\boldsymbol{r}_{ij}))G_{ij}\,\mathrm{e}^{\mathrm{i}\boldsymbol{k}\cdot\boldsymbol{r}_{ij}}, \tag{A.4a}$$

$$B_{\boldsymbol{k}} = \frac{1}{N}\sum_{i,j} J_{ij}\left[(1-\cos(\boldsymbol{Q}\cdot\boldsymbol{r}_{ij}))G_{ij} - (1+\cos(\boldsymbol{Q}\cdot\boldsymbol{r}_{ij}))F_{ij}(1-\mathrm{e}^{\mathrm{i}\boldsymbol{k}\cdot\boldsymbol{r}_{ij}})\right] - \mu, \tag{A.4b}$$

where μ is the Lagrange multiplier for the constraint. The spin-wave spectrum reads

$$\omega_{\boldsymbol{k}} = \sqrt{B_{\boldsymbol{k}}^2 - A_{\boldsymbol{k}}^2}. \tag{A.5}$$

At $T = 0$, where $n_k = 0\ \forall \boldsymbol{k} \neq 0$, one finds that μ vanishes. This also implies the disappearance of the gap at $\boldsymbol{k} = 0$ that may exist for finite temperature. A vanishing gap is a necessary condition for magnetic LRO. It also enables Bose condensation in the $\boldsymbol{k} = 0$ mode. Separating out the contribution of the zero mode, $\langle a^{\dagger}_{\boldsymbol{k}=0} a_{\boldsymbol{k}=0}\rangle/N = \langle a_{\boldsymbol{k}=0} a_{\boldsymbol{k}=0}\rangle/N \equiv M_0$ (corresponding to the magnetic order parameter), one arrives at the zero-temperature equations

$$F_{ij} = M_0 + \frac{1}{2N}\sum_{\boldsymbol{k}\neq 0}\frac{B_{\boldsymbol{k}}}{\omega_{\boldsymbol{k}}}\cos(\boldsymbol{k}\cdot\boldsymbol{r}_{ij}), \tag{A.6a}$$

$$G_{ij} = M_0 + \frac{1}{2N}\sum_{\boldsymbol{k}\neq 0}\frac{A_{\boldsymbol{k}}}{\omega_{\boldsymbol{k}}}\cos(\boldsymbol{k}\cdot\boldsymbol{r}_{ij}), \tag{A.6b}$$

and the constraint of vanishing magnetization at each site becomes

$$S + \frac{1}{2} = M_0 + \frac{1}{2N}\sum_{\boldsymbol{k}\neq 0}\frac{B_{\boldsymbol{k}}}{\omega_{\boldsymbol{k}}}. \tag{A.7}$$

It is not *a priori* clear that the classical ordering vector $\boldsymbol{Q}^{\mathrm{cl}}$ correctly describes the LRO in the quantum system. In order to account for the competition between states with LRO at different ordering vectors $\boldsymbol{Q}$ we extend the MSW procedure by optimizing the free-energy $\mathcal{F}$ with respect to the ordering vector $\boldsymbol{Q}$. This yields two additional equations which must be added to the set of self-consistent equations,

$$\frac{\partial}{\partial Q_x}\mathcal{F} = -\frac{1}{2}\sum_{i,j} J_{ij}\sin(\boldsymbol{Q}\cdot\boldsymbol{r}_{ij})r_{ij}^{x}[F_{ij}^2 + G_{ij}^2] = 0, \tag{A.8a}$$

$$\frac{\partial}{\partial Q_y}\mathcal{F} = -\frac{1}{2}\sum_{i,j} J_{ij}\sin(\boldsymbol{Q}\cdot\boldsymbol{r}_{ij})r_{ij}^{y}[F_{ij}^2 + G_{ij}^2] = 0. \tag{A.8b}$$

In the SATL with NN interactions these simplify to $Q_y = 0$ and

$$Q_x = 2\arccos\left[-\frac{\alpha}{2}\frac{F_{\boldsymbol{\tau}_2}^2 + G_{\boldsymbol{\tau}_2}^2}{F_{\boldsymbol{\tau}_1}^2 + G_{\boldsymbol{\tau}_1}^2}\right], \tag{A.9}$$

where $\boldsymbol{\tau}_1 = (1, 0)$ and $\boldsymbol{\tau}_2 = (1/2, \sqrt{3}/2)$ are the lattice vectors.

The values of F_{ij} and G_{ij} can now be calculated by self-consistently solving equations (A.4)–(A.8). Through Wick's theorem the knowledge of the quantities F_{ij} and G_{ij} allows the computation of the expectation value of any observable.

Spin stiffness. The optimization of the ordering vector allows a straightforward calculation of the spin stiffness, which gives a measure of how stiff magnetic LRO order is with respect to distortions of the ordering vector, and thus provides a fundamental self-consistency check of our approach. In fact, finding a small spin stiffness casts doubt on the reliability of the spin-wave approach in describing such a strongly fluctuating state, and hence suggests that the true ground state might be quantum disordered.

The spin stiffness tensor is defined as $\rho_{\alpha\beta} = \frac{1}{N}\frac{\mathrm{d}^2\mathcal{F}}{\mathrm{d}Q_\alpha \mathrm{d}Q_\beta}|_{\boldsymbol{Q}=\boldsymbol{Q}^0}$, evaluated at the optimized ordering vector $\boldsymbol{Q}^0$. From this we can extract the *parallel spin stiffness* $\rho_\parallel \equiv \frac{1}{2}(\rho_{xx}+\rho_{yy})$ and the *Gaussian spin stiffness* $\Upsilon = \det\rho$.

Since a change in $\boldsymbol{Q}$ affects the correlators F_{ij} and G_{ij}, we must compute Υ self-consistently. After finding the optimal $\boldsymbol{Q}^0$ by the self-consistent procedure described above, we calculate $\frac{1}{N}\mathcal{F}(Q_x, Q_y)$ self-consistently for several fixed ordering vectors $\boldsymbol{Q} = \boldsymbol{Q}^0 + \Delta\boldsymbol{Q}$ and fit a quadratic form to the results. Since the minimum in the free energy can be very shallow, this procedure can be affected by numerical noise. As an approximation to the true spin stiffness, the *partial spin stiffness* $\rho^{\mathrm{partial}}_{\alpha\beta}$ can be computed via the partial derivatives, i.e. without recalculating the self-consistent equations. It reads as

$$\begin{aligned}\rho^{\mathrm{partial}}_{\alpha\beta} &\equiv \frac{1}{N}\frac{\partial^2}{\partial Q_\alpha \partial Q_\beta}\mathcal{F} \\ &= -\frac{1}{2N}\sum_{i,j} J_{ij}\cos(\boldsymbol{Q}\cdot\boldsymbol{r}_{ij}) r^\alpha_{ij} r^\beta_{ij}[F^2_{ij}+G^2_{ij}]. \end{aligned} \tag{A.10}$$

We define $\Upsilon^{\mathrm{partial}}$ analogously to Υ as the determinant of the partial spin-stiffness tensor.

References

[1] Dyson F J, Lieb E H and Simon B 1978 *J. Stat. Phys.* **18** 335
[2] Kennedy T, Lieb E H and Shastry B S 1988 *J. Stat. Phys.* **53** 1019
[3] Manousakis E 1991 *Rev. Mod. Phys.* **63** 1
[4] Misguich G and Lhuillier C 2004 *Frustrated Spin Systems* ed H T Diep (Singapore: World Scientific) p 229
[5] Anderson P 1973 *Mater. Res. Bull.* **8** 153
[6] Fazekas P and Anderson P W 1974 *Phil. Mag.* **30** 423
[7] Kastner M A, Birgeneau R J, Shirane G and Endoh Y 1998 *Rev. Mod. Phys.* **70** 897
[8] Lee P A, Nagaosa N and Wen X-G 2006 *Rev. Mod. Phys.* **78** 17
[9] de la Cruz C *et al* 2008 *Nature* **453** 899
[10] Coldea R, Tennant D A, Tsvelik A M and Tylczynski T 2001 *Phys. Rev. Lett.* **86** 1335
[11] Shimizu Y, Miyagawa K, Kanoda K, Maesato M and Saito G 2003 *Phys. Rev. Lett.* **91** 107001
[12] Yamashita S, Nakazawa Y, Oguni M, Oshima Y, Nojiri H, Shimizu Y, Miyagawa K and Kanoda K 2008 *Nat. Phys.* **4** 459
[13] Carretta P, Papinutto N, Melzi R, Millet P, Gonthier S, Mendels P and Wzietek P 2004 *J. Phys.: Condens. Matter* **16** S849
[14] Nath R, Tsirlin A A, Rosner H and Geibel C 2008 *Phys. Rev.* B **78** 064422
[15] Weihong Z, McKenzie R H and Singh R R P 1999 *Phys. Rev.* B **59** 14367
[16] Yunoki S and Sorella S 2006 *Phys. Rev.* B **74** 014408
[17] Weng M Q, Sheng D N, Weng Z Y and Bursil R J 2006 *Phys. Rev.* B **74** 012407
[18] Fjaerestad J O, Zheng W, Singh R R P, McKenzie R H and Coldea R 2007 *Phys. Rev.* B **75** 174447
[19] Kohno M, Starykh O A and Balents L 2007 *Nat. Phys.* **3** 790

[20] Starykh O A and Balents L 2007 *Phys. Rev. Lett.* **98** 077205
[21] Heidarian D, Sorella S and Becca F 2009 *Phys. Rev.* B **80** 012404
[22] Singh R R P, Weihong Z, Hamer C J and Oitmaa J 1999 *Phys. Rev.* B **60** 7278
[23] Capriotti L, Becca F, Parola A and Sorella S 2001 *Phys. Rev. Lett.* **87** 097201
[24] Sushkov O P, Oitmaa J and Weihong Z 2001 *Phys. Rev.* B **63** 104420
[25] Sindzingre P 2004 *Phys. Rev.* B **69** 094418
[26] Sirker J, Weihong Z, Sushkov O P and Oitmaa J 2006 *Phys. Rev.* B **73** 184420
[27] Mambrini M, Läuchli A, Poilblanc D and Mila F 2006 *Phys. Rev.* B **74** 144422
[28] Darradi R, Derzhko O, Zinke R, Schulenburg J, Krueger S E and Richter J 2008 *Phys. Rev.* B **78** 214415
[29] Takahashi M 1989 *Phys. Rev.* B **40** 2494
[30] Xu J H and Ting C S 1991 *Phys. Rev.* B **43** 6177
[31] Hauke P, Roscilde T, Murg V, Cirac J I and Schmied R 2010 *New J. Phys.* **12** 053036
[32] Figueirido F, Karlhede A, Kivelson S, Sondhi S, Rocek M and Rokhsar D S 1989 *Phys. Rev.* B **41** 4619
[33] Read N and Sachdev S 1991 *Phys. Rev. Lett.* **66** 1773
[34] Ferrer J 1993 *Phys. Rev.* B **47** 8769
[35] Manuel L O and Ceccatto H A 1999 *Phys. Rev.* B **60** 9489
[36] Schmied R, Roscilde T, Murg V, Porras D and Cirac J I 2008 *New J. Phys.* **10** 045017
[37] Schulenburg J and Richter J 2010 *Eur. Phys. J.* B **73** 117
[38] Weber C, Läuchli A, Mila F and Giamarchi T 2006 *Phys. Rev.* B **73** 014519
[39] Singh R R P 1989 *Phys. Rev.* B **39** 9760
[40] Capriotti L, Trumper A E and Sorella S 1999 *Phys. Rev. Lett.* **82** 3899
[41] White S R and Chernyshev A L 2007 *Phys. Rev. Lett.* **99** 127004
[42] Sandvik A 1997 *Phys. Rev.* B **56** 11678
[43] Zheng W, Fjaerestad J O, Singh R R P, McKenzie R H and Coldea R 2006 *Phys. Rev.* B **74** 224420
[44] Chubukov A V, Sachdev S and Senthil T 1994 *J. Phys.: Condens. Matter* **6** 8891
[45] Chernyshev A L and Zhitomirsky M E 2009 *Phys. Rev.* B **79** 144416
[46] Gazza C J and Ceccatto H A 1993 *J. Phys.: Condens. Matter* **5** L135
[47] Trumper A E 1999 *Phys. Rev.* B **60** 2987
[48] Sandvik A W and Evertz H G 2010 *Phys. Rev.* B **82** 024407
[49] Lecheminant P, Bernu B, Lhuillier C and Pierre L 1995 *Phys. Rev.* B **52** 9162
[50] Shastry B S and Sutherland B 1990 *Phys. Rev. Lett.* **65** 243
[51] Kawamura H 2002 arXiv:cond-mat/0202109v1
[52] Richter J, Gros C and Weber W 1991 *Phys. Rev.* B **44** 906
[53] Gelfand M P, Singh R R and Huse D A 1989 *Phys. Rev.* B **40** 10801
[54] Moreo A, Dagotto E, Jolicoeur T and Riera J 1990 *Phys. Rev.* B **42** 6283
[55] Chubukov A 1991 *Phys. Rev.* B **44** 392
[56] Leung P W and Lam N 1996 *Phys. Rev.* B **53** 2213
[57] Chandra P and Doucot B 1988 *Phys. Rev.* B **38** 9335
[58] Locher P 1990 *Phys. Rev.* B **41** 2537
[59] Zhong Q F and Sorella S 1993 *Europhys. Lett.* **21** 629
[60] Capriotti L, Scalapino D J and White S R 2004 *Phys. Rev. Lett.* **93** 177004
[61] Capriotti L and Sachdev S 2004 *Phys. Rev. Lett.* **93** 257206
[62] Murg V, Verstraete F and Cirac J I 2009 *Phys. Rev.* B **79** 195119
[63] Nishimori H and Saika Y 1990 *J. Phys. Soc. Japan* **59** 4454
[64] Barabanov A F and Starykh O A 1990 *JETP Lett.* **51** 311
[65] Xu J H and Ting C S 1990 *Phys. Rev.* B **42** 6861
[66] Ivanov N B and Ivanov P C 1992 *Phys. Rev.* B **46** 8206
[67] Gochev I G 1994 *Phys. Rev.* B **49** 9594
[68] Dotsenko A V and Sushkov O P 1994 *Phys. Rev.* B **50** 13821

[69] Einarsson T and Schulz H J 1995 *Phys. Rev.* B **51** 6151
[70] Schulz H, Ziman T and Poilblanc D 1996 *J. Physique* I **6** 675
[71] Trumper A E, Manuel L O, Gazza C J and Ceccatto H A 1997 *Phys. Rev. Lett.* **78** 2216
[72] Manuel L O, Trumper A E and Ceccatto H A 1998 *Phys. Rev.* B **57** 8348
[73] Bonča J, Rodriguez J P, Ferrer J and Bedell K S 1994 *Phys. Rev.* B **50** 3415
[74] Dyson F J 1956 *Phys. Rev.* **102** 1217
[75] Maleev S V 1957 *Zh. Eksp. Teor. Fiz.* **30** 1010
see also Maleev S V 1958 *Sov. Phys.—JETP* **6** 776
[76] Fetter A and Walecka J 1971 *Quantum Theory of Many-Particle Systems* (New York: McGraw-Hill)